Journal of Nanobiotechnology

RESEARCH Open Access

Black phosphorus nanosheets encapsulated microneedle for multifunctional therapy for androgenic alopecia

Sha Xiong[1†], Zhongjun Li[2†], Siwen Jiao[1], Ting Xiao[1], Yan Wu[1], Chen Chen[1], Shiqi Guo[1], Xiaojuan Li[1], Zhiyuan Pan[2], Jianqing Li[2] and Yuehong Xu[1*]

Abstract

Background Androgenetic alopecia (AGA), a chronic and progressive disease, significantly impacts the patients' social, emotional, and mental well-being. Current treatment for AGA are mainly limited by drug side effects and the stratum corneum (SC) barrier of scalp.

Results To address these issues, we developed a microneedle (MN) system loaded with black phosphorus nanosheets (BP) encapsulating baicalin (BA), a natural ingredient, for effective treatment of AGA. We first fabricated BP-BA based on the BP properties of high drug loading capacity and excellent photothermal conversion efficiency. Upon 635 nm laser irradiation, BP-BA demonstrated efficient photothermal conversion to mild thermal of ~ 42 °C. This mild thermal effect controlled BA's stimuli-responsive release, enhanced cellular uptake, and effectively modulated gene expression in dihydrotestosterone-treated human dermal papilla cells, downregulating negative regulators such as SRD5A2, AR, DKK1, and TGFB1, while upregulating positive regulators like CTNNBIP1 and VEGFA. Furthermore, we encapsulated BP-BA to MN fabricating BP-BA@MNs to overcome the SC barrier. Compared with BP-BA@MNs without laser irradiation, BP-BA@MNs with laser irradiation significantly enhanced drug penetration into the subcutaneous area and accumulation at the follicular site. Importantly, BP-BA@MNs demonstrated synergistic efficacy against testosterone-induced AGA in vivo through combining BA chemotherapy, BP-mediated mild photothermal therapy, and MN delivery, as well as good biocompatibility and biosafety, and the underlying synergistic mechanism was elucidated in terms of follicular microenvironment reconstruction.

Conclusions This combining BP mild photothermal and MN system is a promising approach for follicular targeted drug delivery, providing a multifunctional strategy for addressing the clinical needs of anti-AGA.

Keywords Baicalin, Black phosphorus nanosheets, Mild thermal, Microneedles, Follicular targeted drug delivery, Androgenetic alopecia

Background

Androgenetic alopecia (AGA) is a chronic and progressive hair loss, with a high incidence in clinical practice, globally affecting approximately 86.4 of men and 30.7% of women [1, 2]. The pathogenesis of AGA involves multiple factors, including androgen level, genetics, gender, and age, which significantly impair the quality of life and mental health of affected individuals [3]. The primary pathophysiological mechanisms underlying AGA include an

†Sha Xiong and Zhongjun Li have contributed equally to this work.

*Correspondence:
Yuehong Xu
lssxyh@mail.sysu.edu.cn
[1] School of Pharmaceutical Sciences, Sun Yat-Sen University, Guangzhou 510006, China
[2] Faculty of Innovation Engineering, Macau University of Science and Technology, Macau 999078, China

heightened androgenic milieu and vascular insufficiency in the scalp. Specifically, the overexpressed 5α-reductase, increased androgen receptors (ARs), and elevated dihydrotestosterone (DHT) production lead to the progressive miniaturization of hair follicles (HFs). Concurrently, vascular insufficiency compromised nutrient delivery to HFs. These disruption collectively shorten the anagen phase of hair growth cycle, resulting in hair thinning and eventual hair loss. Currently, the available treatments approved by the Food and Drug Administration (FDA) for AGA are only topical minoxidil (MXD, a vasodilator medication), oral finasteride (FIN, a 5α-reductase inhibitor), and low-level laser therapy (LLLT) [4, 5]. Alternative treatments, such as botulinum toxin injection, platelet-rich plasma therapy, stem cell therapy, and hair transplant etc. were developed for addressing the unmet needs for AGA therapy [6, 7]. However, these treatments are limited by systemic side effects, insufficient efficacy, poor patient compliance, and high cost [8]. Given the intricate pathophysiology of AGA and the limitations of current treatments, there is an urgent need for developing a safe and effective combination therapies. Among them, topical drug intervention is fundamental with good patient compliance.

Baicalin (BA), a flavone glycoside extracted from the Chinese herb *Scutellaria baicalensis*, is a well-known active ingredient against various inflammatory diseases and possesses good anti-AGA properties [9]. It has been reported to promote hair regrowth in mice by activating the Wnt/β-catenin signaling pathway and enhancing the activity of dermal papilla cells (DPCs) [10, 11]. Moreover, BA exhibits biological activities against androgen-associated disorders, such as prostate cancer and acne. It inhibited the production of DHT and the activity of 5α-reductase Type II (SRD5A2) in the testosterone-induced animal model, and also suppressed the AR mRNA expression in DHT-treated prostate epithelial RWPE-1 cells and prostate stromal cell WPMY-1 [12]. Despite its therapeutic potential, BA's application is hindered by its poor water solubility (~67 μg/mL) and inadequate permeability ($Papp = 0.037 \times 10^{-6}$ cm/s) [13]. To improve its bioavailability, different nanoformulations have been developed, including BA-loaded phospholipid vesicles and micelles, aimed at overcoming these limitations and promoting hair regeneration [14, 15]. However, these nanoformulations face challenges such as low drug-loading capacity and poor entrapment efficiency.

Black phosphorus (BP), as a rising star in two-dimensional (2D) materials, has garnered significant attention in drug delivery due to its high drug loading capacity, excellent photothermal conversion efficiency, and favorable biocompatibility and biodegradation [16]. The high drug loading capacity attributes to BP's large surface area. BP degrades into biocompatible phosphorus oxides, ensuring negligible toxicity within living organisms [17]. To date, BP-based drug delivery systems (DDS) were emerging especially for cancer therapy due to their excellent properties with photothermal/photodynamic therapy (PTT/PDT) capabilities and stimuli-responsive controlled drug release [18]. For skin diseases, BP-based DDS have been reported for skin tumors and wound healing [19, 20]. However, its potential in treating hair-related diseases remains unexplored. BP has the advantage of possessing a wider layer-tunable energy bandgap that allows it to efficiently absorb light across a wide range, from ultraviolet to infrared spectrums [21]. This property makes BP suitable for utilizing its photothermal conversion efficacy, especially with 635 nm laser irradiation, which produces a mild photothermal effect (approximately 42 ℃). Interestingly, non-invasive LLLT using wavelengths between 630 and 660 nm has been approved by the FDA for an adjunctive anti-AGA therapy since 2007 [22, 23]. Inspired by this, we hypothesize that the similar wavelength of 635 nm irradiation on BP presents a beneficial effect on promoting hair regeneration. Furthermore, BP-mediated mild photothermal conversion can enhance cell proliferation, improve subcutaneous blood flow, stimulate HF circulation, and enhance drug penetration. Therefore, we anticipate that BP may efficiently load BA to fabricate BP-BA nanoparticles, which may exhibit a combination therapy for AGA through BA chemotherapy and the mild thermal effect of 635 nm laser irradiation. However, for effective AGA treatment, a promising drug delivery system must enhance drug retention in the HFs. Thus, BP-BA must overcome the stratum corneum (SC) barrier to be delivered to the follicular site.

In recent year, many strategies have been explored to overcome the SC barrier and enhance local intercutaneous penetration [24, 25]. Microneedles (MNs), as an effective drug delivery system between patches and subcutaneous injections, primarily create multiple transient microchannels by reversibly puncturing the SC barrier, thereby delivering more drugs into the dermis [26]. The emerging application of MNs is attributed to its various excellent properties, including minimal invasiveness, convenience, high efficiency, and safety [27]. MNs have been reported to deliver drugs for treating various skin diseases, such as melanoma [28], scar [29, 30], psoriasis [31], as well as AGA or alopecia areata [32–36]. Previously, we reported the use of MN to deliver FIN-loaded lipid nanocarriers (FIN-NLC) to the deep skin layer, where FIN-NLC further specifically delivered FIN to HFs to promote hair growth in AGA [37]. Therefore, we further fabricated an MN patch encapsulating BP-BA (BP-BA@MNs). It is hypothesized that BP-BA@MNs

can efficiently deliver BP-BA to the HF site, BP-BA will release more BA retention in the HF with the assistance of mild PT, and eventually the system provides a multi-functional strategy of combining BA, BP, and MNs to address the clinical needs of anti-AGA (Fig. 1).

Herein, we firstly fabricated BP-BA to improve the solubility of BA (~ 12-fold) and increase its drug loading (74.49%), and then integrated BP-BA into MNs. BP-BA exhibited PT effect upon 635 nm laser irradiation. The *in vitro* anti-AGA efficacy in DHT-treated hDPCs of BP-BA with 635 nm laser irradiation was evaluated through downregulating *SRD5A2*, *AR*, *DKK1*, and *TGFB1* and upregulating *CTNNBIP1* and *VEGFA*. BP-BA@MNs with 635 nm irradiation

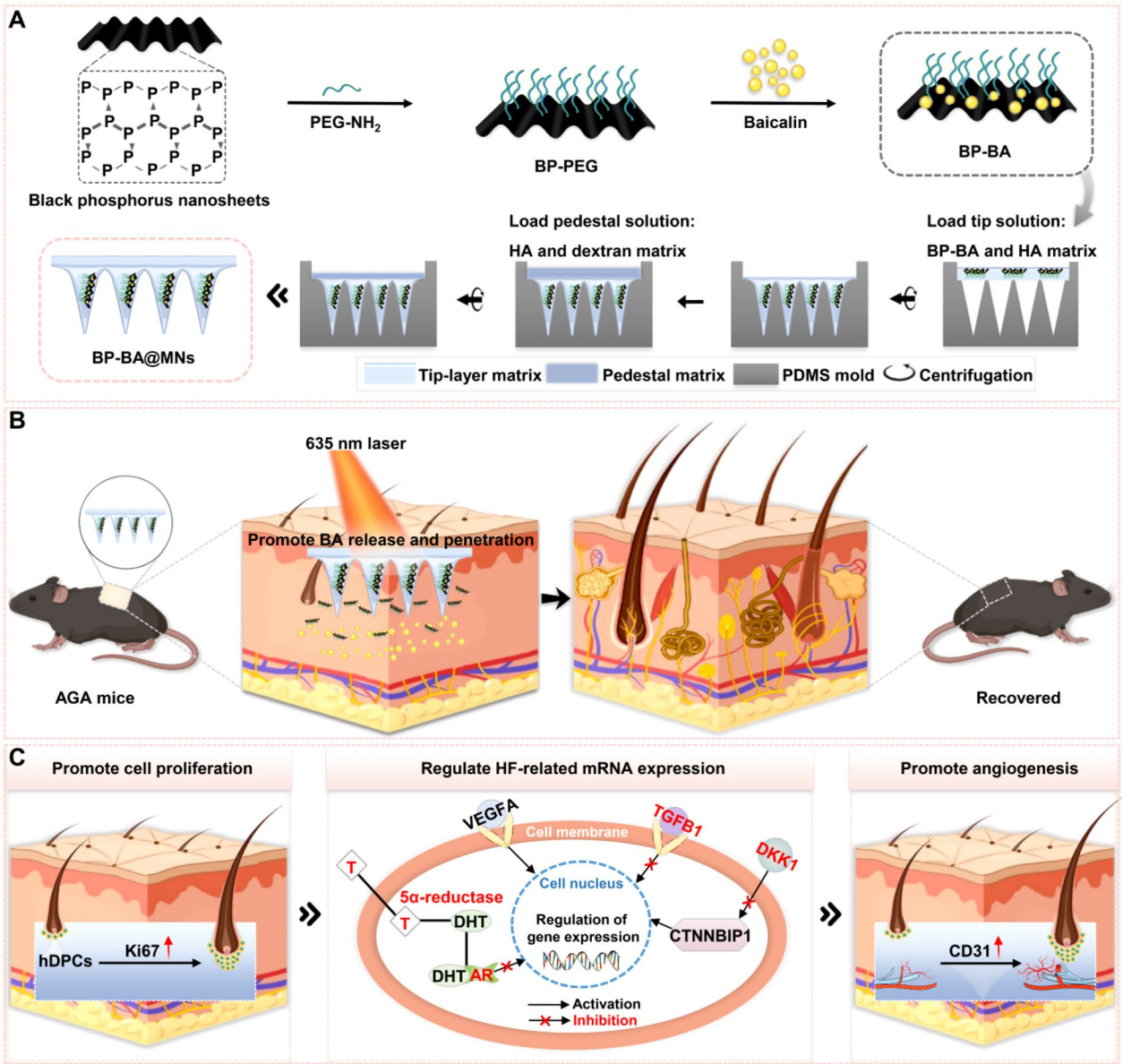

Fig. 1 Schematic illustration of BP-BA@MNs with 635 nm irradiation for anti-AGA. **A** Fabrication of BP-BA and BP-BA@MNs. The BP-BA was fabricated through the electrostatic interaction between BP-PEG and BA, and BP-BA@MNs were further fabricated using a micromold method. **B** BP-BA@MNs enhanced the delivery of BP-BA to the HF site and the release of BA combining PT and MN. **C** The effects of BP-BA@MNs on the treatment of AGA through promoting cell proliferation of hDPCs, regulating HF-related mRNA expression, and promoting angiogenesis. AGA, androgenic alopecia; AR: androgen receptor; BA: baicalin; BP: black phosphorus nanosheets; BP-BA: baicalin-loaded black phosphorus nanosheets; DHT: dihydrotestosterone; hDPCs: human dermal papilla cells; HF: hair follicle; MN: microneedle; BP-BA@MNs: baicalin-loaded black phosphorus nanosheets encapsulated microneedles; PT: photothermal; T: testosterone

significantly delivered more drug to HFs in comparison with BP-BA with 635 nm irradiation and BP-BA@MNs without 635 nm irradiation, they exhibited penetration enhancement combining PT and MN. More importantly, in a testosterone-induced AGA animal model, BP-BA@MNs with 635 nm irradiation exhibited a synergistic effect of the combination of BA, BP, and MN, and promoted hair regeneration by normalizing the HF microenviroment damaged by androgen and activating perifollicular angiogenesis.

Methods and materials

Materials

Bulk BP was obtained from Smart-Elements (Austria). N-methyl-2-pyrrolidone (NMP) (99.5%, anhydrous) was purchased from Aladdin Reagents (Shanghai, China). Baicalin (BA), and NH_2-PEG were purchased from Macklin (Shanghai, China). HA (55 kDa and 200–400 kDa) was obtained from Freda (Shandong, China). Dextran (40 kDa) was obtained from Aladdin (Shanghai, China). Coumarin 6 (C6) was bought from Sigma-Aldrich (St Louis, MO, USA). hDPCs was obtained from Shanghai Sixin Biotechnology Co., Ltd. (Shanghai, China). MitoTracker™ Red was obtained from Invitrogen (OR, USA). 4′,6-diamidino-2-phenylindole (DAPI) was obtained from Sevier (Wuhan, China). Dulbecco's modified Eagle's medium (DMEM) and fetal bovine serum (FBS) were purchased from Gibico (Gaithersburg, MD, USA). 3-(4,5)-dimethylthiahiazo (-z-y1)-3,5-di- phenytetrazoliumromide (MTT) was obtained from Solarbio (Beijing, China). 5% (w/v) minoxidil tincture (MXD) was purchased from Wansheng Pharmaceutical Co., Ltd. (Zhejiang, China). Testosterone and DHT was obtained from Energy Chemical (Shanghai, China). The antibodies of anti-β-catenin, anti-Ki67, and anti-CD31 were purchased from Servicebio (Guangzhou, China). All other reagents were analytical grade or better.

Synthesis of BP nanosheets

BP was prepared by liquid phase exfoliation [38]. Briefly, 0.1 g of bulk BP in a volume of 10 mL was thoroughly ground in an agate mortar to obtain a uniformly suspension. The mixture was then processed in an ultrasonic cleaner (power: 300 W) for 48 h at a constant temperature of 10 °C maintained by a circulating water condenser. Afterwards, the mixture was centrifuged at 9000 rpm for 5 min. Following this, a further 5 min of centrifugation at 12,000 rpm was performed on the supernatant. The pelleted material was resuspended in NMP to obtain a suspension of BP nanosheets, hereafter referred to simply as BP.

Synthesis of BP-BA

To prepare BP-BA, 10 mg PEG-NH_2 was initially added to 2 mL of aqueous BP at a concentration of 50 μg/mL and stirred at 300 rpm for 6 h. The product with the amino end of BP (BP-PEG) was obtained by centrifuged at 13,000 rpm for 20 min. Afterwards, the BP-PEG was then dispersed in 1 mL of DMSO solution, and further 1 mL of BA at a concentration of 400 μg/mL was added to the BP-PEG under a magnetic stirrer, and the electrostatic interaction was carried out at room temperature for 3 h. The obtained BP-BA was centrifuged at 13,000 rpm for 20 min and washed three times with ultrapure water and stored at 4 ℃.

Characterization of BP preparations

BP preparations were characterized with transmission electron microscopy (TEM), atomic force microscopy (AFM), X-ray diffraction (XRD), and Raman spectrum analysis. An electron microscope (HT7700, Hitachi) was used to collect TEM images at an accelerating voltage of 80.0 kV and an emission current of 10.0 μA. An XRD measure was obtained by a micro XRD device (D8 Discover, Bruker) operated at 45 kV and 100 mA (Cu-Kα radiation). BP-PEG preparations were characterized via TEM, HRTEM, and energy-dispersive X-ray spectroscopy (EDS) element mapping. EDS element mapping was conducted using the scanning TEM (STEM) mode of a TEM (JEM-F200, JEOL). BP-BA preparations were characterized with Fourier transform infrared spectroscopy (FTIR), hydrogen nuclear magnetic resonance (^{1}H NMR) spectra, and dynamic light scattering (DLS). The FTIR was conducted using a Perkin Elmer (L16000300 Spectrum TWO LITA, Llantrisant, UK) from 1400 to 600 cm^{-1} via the potassium bromide (KBr) pellet method. ^{1}H NMR was performed using a NMR (NMR, 400 MHz, Avance III; Bruker Optik GmbH, Ettlingen, German). Dynamic light scattering (DLS) was performed on a Malvern Zetasizer Nano S (Malvern Instruments Ltd., UK) to determine the zeta potential and hydrodynamic size of BP-BA.

PT performance assessment

BP suspension of 10 mL was centrifuged at 18,000 rpm for 30 min. After removing the supernatant, the precipitate was dried under vacuum at 80 °C or 2 h. Weighing the dried sample determined the BP concentration. A series of aqueous BP solutions with concentrations of 0, 5, 10, 20, 50 μg/mL were prepared. The PT performance was immediately measured, followed by an analysis of the temperature curves. BP-BA was performed using the same methods.

The temperature of different preparations was measured using a thermocouple after irradiation with a 635 nm laser (power density: 0.5 W/cm^2). To regulate the temperature distribution in the laser area, a collimator was used to add the compound of interest to a quartz cell with high red light transmittance. Time-[-Ln(θ)] scatter was linearly fitted and the resultant slope and other parameters were incorporated into the following formula (1) as a means of calculating photothermal conversion efficiency (PCE):

$$\eta = \frac{hA\Delta T_{max} - Q}{I\left(1 - 10^{-A_\lambda}\right)} \quad (1)$$

where η is PCE, h is the heat transfer coefficient of the dispersed PT, A is the container surface area, ΔT_{max} is the maximum temperature elevation under light irradiation, I is the irradiated light power, A_λ is the absorbance of the PT agent upon 635 nm irradiation, Q is the heat absorbed by the pure dispersion liquid ($I \times 5.4$ mW for deionized water).

In vitro release study

BA release from BP-BA or BP-BA + 635 nm was performed by the modified horizontal Franz-type diffusion cell method [39]. The donor and receptor compartment were separated by a dialysis membrane with a molecular weight cutoff of 2000 Dalton. The donor compartment was loaded with 1.0 ml of either BA suspension or BP-BA suspension (containing an equivalent BA dose of 380 μg). The receptor compartment contained 8 mL of dissolution medium comprising 30% (w/v) polyethylene glycol 400 in normal saline, which maintained the sink condition. The medium in the receptor compartment was continuously stirred at 250 rpm and 32 ± 0.5 ℃. At predetermined time intervals, 1 mL of sample was withdrawn from the receptor compartment and replaced immediately with an equal volume of blank medium to maintain a constant volume. For the BP-BA exposed to 635 nm laser irradiation, BP-BA was irradiated with 635 nm laser for 3 min (0.5 W/cm^2) prior to the beginning of the test process. All the withdrawn samples were filtered through 0.22 μm filter membranes and analyzed using the high-performance liquid chromatography (HPLC). A Cosmosil C18 reverse phase column (5 mm, 4.6 mm inner diameter × 25 cm; Dikma Technologies, Inc., Beijing, China) was used. The mobile phase consisted of methanol:water:phosphoric acid (47:53:0.2, v/v) with a flow rate of 1 mL/min, and the detection wavelength was set at 280 nm.

Cellular experiments

MTT assay

We conducted an MTT assay to evaluate the cytotoxicity of BA and BP-BA with or without 635 nm laser irradiation (0.5 W/cm^2, 3 min) on hDPCs. Briefly, the cells were seeded in 96-well plates at a density of 10×10^3 cells per well. In addition to the control, the cells were then exposed to BA, BP-BA, BP-BA + 635 nm with various concentrations of BA (1, 5, 10, 20, 50, 100, 200 μM). The exposure time to the test substances was 24 h. At the end of the exposition time, the medium was removed and 100 μL of 1 mg/mL of MTT solution was added to each well and then incubated at 37 °C for 4 h. Finally, the supernatant was removed and the formazan crystals were dissolved in 150 μL of DMSO after 8-min incubation. The absorbance was measured at 490 nm using a microplate reader (FluoroMax-4, HORIBA).

Additionally, the effects of these preparations on a dihydrotestosterone (DHT)-induced AGA cell model were evaluated in vitro. The hDPCs were seeded in 96-well plates (10×10^3/per well) and left for 24 h to attach. The cells were then pretreated with BA, BP-BA, and BP-BA + 635 nm (containing BA of 1, 5, 10, 20, and 50 μM) for 4 h. Subsequently, the cells were incubated with 1 μM DHT for an additional 24 h based on our previous work [40]. The cells without any treatment served as the control, and the cells incubated only with 1 μM DHT served as the model. The cytotoxicity of BA, BP-BA, and BP-BA + 635 nm was then investigated following the same MTT assay procedure as described above.

Polymerase chain reaction (PCR) assay

We digested hDPCs in the logarithmic growth phase with trypsin and fully suspended them in DMEM medium. After that, 10 μL of cell suspension were pumped into the blood counting chamber for counting. As a control, DMEM medium was seeded in 12-well plates with 30×10^4 hDPCs per well. After 24 h, the medium was removed, and 1 μM of DHT solution was added to each well. Subsequently, BA, and BP-BA suspension with or without 635 nm laser irradiation containing an equivalent concentration of 20 μM BA were added to the respective wells. After an additional 24 h incubation, the cells were washed thoroughly three times with precooled phosphate buffered saline (PBS). Total RNA was extracted with the Trizol reagent (Invitrogen, Thermo Fisher Scientific, Inc., Waltham, MA, USA), and reverse transcription was performed using the PrimeScript RT-PCR kit (Takara, Dalian, China) according to the manufacturer's protocol. RT-PCR was performed with the SYBR PrimeScript RT-PCR kit (Takara), Power SYBR Green PCR Master Mix, and a real-time PCR Cycler (Roche LightCycle 480II,

Table 1 Primer sequences used for quantitative real time PCR in hDPCs

Gene	Forward primer (5′-3′)	Reverse primer (5′-3′)
GAPDH	TGAAGGTCGGAGTCAACGG	TGGAAGATGGTGATGGGAT
SRD5A2	GCTTCATACCCACTCCCTGT	TGGGTCTTTGTGGCTTCAGA
AR	GGGACCATGTTTTGCCCATT	GCAGCTTCCACATGTGAGAG
DKK1	TGATGAGTACTGCGCTAGTC	CTCCTATGCTTGGTACACAC
TGFB1	AGACTTTTCCCCAGACCTCG	TGGGTGGTCTTGAATAGGGG
CTNNBIP1	AAGCAGAGATGGCCCAGAAT	AGTGGGATGGTGGGTGTAAG
VEGFA	AGGGCAGAATCATCACGAAGT	AGGGTCTCGATTGGATGGCA

BIOTECON Diagnostics). Table 1 lists the sequences of the specific primers (Sangon Biotech, Shanghai, China) used in RT-PCR. PCR was performed for 40 cycles, and the relative expression levels of *SRD5A2*, *AR*, *DKK1*, *TGFB1*, *CTNNBIP1*, and *VEGFA* mRNA were quantitated using $2^{-\Delta\Delta Ct}$ method.

Intracellular uptake and tracking

hDPCs were cultured in 10 mm^2 confocal wells at a density of 10×10^4 cells/well in DMEM medium. After 24 h, the medium was removed, and the cells were washed with PBS and stained with Mito Tracker for 1 h. Following three additional washes with PBS, the cells were incubated with either free C6, or BP-C6 with or without 635 nm laser irradiation (the concentration of C6 is the same with 100 ng/mL) for 4 h. Next, the cells were washed with PBS and fixed with paraffin for 15 min. The wells were again washed with precooled PBS three times, and then DAPI was used to stain the cell nuclei. Finally, all samples were imaged using a confocal laser scanning microscope (CLSM; Olympus FV300, Japan) to visualize the cellular internalization and localization of C6.

Mice vibrissa HF organ culture ex vivo

Five-week-old male C57BL/6 mice were euthanized, and their HFs were dissected from their whisker pads. Each isolated HF was placed to a separate well of a 48-well plate containing 500 μL DMEM culture medium. The basic culture medium described above was supplemented with five treatment conditions: (1) a non-treated control group, (2) 8 μM DHT, (3) 8 μM DHT + BA, (4) 8 μM DHT + BP-BA, and (5) 8 μM DHT + BP-BA + 635 nm irradiation. In groups 3, 4, 5, the concentration of BA remained constant at 20 μM. The HFs were cultured under each condition and kept free-floating in a humidified incubator at 37 °C, 5% CO_2, and 95% air. The medium was changed and the inversion microscope images were taken every three days, and the lengths of vibrissae follicles were measured using Image J software on day 12.

Preparation and characterization of BP-BA@MNs

The BP-BA@MNs matrix solution was fabricated as follows. Briefly, HA (52 kDa) was dissolved in 1 mL of water to prepare a blank tip-layer matrix solution, and BP-BA was then added and mixed uniformly to produce tip-layer solution. To prepare the pedestal matrix solution, 0.10 g of HA (52 kDa) and 0.10 g of HA (200–400 kDa) were dissolved in 1 mL of a 10% (w/v) dextran 40 solution.

BP-BA@MNs were fabricated as previously [37]. The master mold consisted of 144 stainless pyramidal molds with a height of 800 μm, a base of 200 μm, and an interspacing of 400 μm. Polydimethylsiloxane (PDMS) was cast over the master mold, degassed in a vacuum desiccator for 1 h, cured in a 95 ℃ oven for 30 min for solidification, and then peeled off to obtain the inverse mold. BP-BA@MNs were fabricated using this PDMS inverse mold through a two-step molding process. In the first step, 0.05 g of tip-layer solution was dipped into the mold and centrifuged at 3000 rpm for 4 min while rotating the mold 180° to ensure even filling. In the second step, 0.12 g of pedestal solution was cast onto the surface of the tip layer and centrifuged at 3000 rpm for another 4 min. After this, the pedestal was rotated 180° until it was evenly paved. After drying for 48 h at 4 ℃ in a vacuum desiccator, the PDMS mold was peeled off to obtain BP-BA@MNs.

The BP-BA@MNs were morphologically characterized using a digital optical microscope (Nikon-Ts2R-FL; Japan). A confocal laser scanning microscope (CLSM) was used to observe the drug distribution in the MN by loading BP-C6 into the MNs following the same fabrication protocol as for BP-BA@MNs. The mechanical strength of the BP-BA@MNs was measured with the XT-plus Texture Analyzer (Stable Micro System, Surrey, UK). To evaluate the insertion depth, ten layers of Parafilm M® sheets were stacked to simulate skin, and the insertion depth of BP-BA@MNs through the film was assessed. BP-BA@MNs loaded with 0.2%, (w/w) methylene blue were inserted into isolated rat skin, and the integrity and sealing of the microchannels formed in the skin were assessed after removing the MN array. Additionally, the depth of penetration of BP-BA@MNs in isolated rat skin tissues was assessed using optical coherence tomography (OCT; EX1301 OCT microscope, Michelson Diagnostics, Kent, UK).

HF permeability

The SD rats were anesthetized with urethane (20%, w/v) and the abdomen hairs were removed using a depilatory cream (Veet, London, UK). The SC recovered for 24 h. After that, the rats were randomized into five groups (n = 3/group): (1) Free C6, (2) BP-C6,

(3) BP-C6 + 635 nm irradiation, (4) BP-C6@MNs, and (5) BP-C6@MNs + 635 nm irradiation. Animals were topically administered with the indicated treatments (Equivalent to 200 ng of C6, 20 μg of BP). For the group 4 and group 5, MNs were inserted into the skin with a force of 30 N for 5 min, and subsequently the group 3 and group 5 underwent 635 nm irradiation (0.5 W/cm^2; 3 min), and finally covered with a tape (Scotch Transparent Tape; 3 M, St. Paul, USA). After 4 h of permeation, the tape was removed and the skin was cleaned and removed. The permeated skins were imaged using CLSM, and the C6 fluorescence was measured using Image J software.

In vivo pharmacodynamical studies

Establishment and treatment of the testosterone-induced AGA mice

Animal studies were conducted using 6–8 week-old male C57BL/6 mice (24–26 g) those were housed in a standard environmentally controlled (25 ± 2 °C, 55 ± 5% relative humidity, 12 h light/dark cycle) facility with free access to food and water. The actions were taken in compliance with Sun Yat-sen University's regulations on animal welfare. All the animal experiment protocols were approved by the ethics committee at Sun Yat-sen University.

The hairs on the dorsal skin of C57BL/6 mice were depilated with an area of 2 cm by 3 cm, then the mice were randomized into the following groups (n = 6/group): (1) control group, (2) testosterone group (used as the model for AGA), (3) MXD group (positive control, treated with commercial minoxidil tincture), (4) BA group (treated with BA), (5) BP-BA group (treated with BP-BA, without laser irradiation), (6) BP-BA + 635 nm group (treated with BP-BA and irradiated with 635 nm laser), (7) Blank MNs group (treated with blank MNs), (8) BP-BA@MNs group (treated with BP-BA@MNs, without laser irradiation), and (9) BP-BA@MNs + 635 nm (treated with BP-BA@MNs and irradiated with 635 nm laser). Except for the control group, all animals were topically administered with 0.1 mL testosterone solution (0.2%, w/v) daily on the depilated skin for 28 consecutive days to establish the AGA model [41]. On day 28 post-modeling, the dorsal skin was shaved again and recovered for 24 h. The model group continued to receive the testosterone solution daily for an additional 15 days. Animals in group 3 were topically administered with 0.1 mL commercial minoxidil tincture daily (5%, w/v) for 15 days. Each animal in groups 4, 5, and 6 was topically administered with 0.1 mL of the corresponding preparations daily (containing an equivalent BA dose of 100 μmoL) for 15 days. In group 6, the animal was irradiated with 635 nm laser at 0.5 W/cm^2 for 3 min once every three days after the BP-BA was administered for 30 min. Each animal in groups 7, 8, and 9 was administered with one corresponding MN patch on day 0, 3, 6, 9, 12. In group 9, the animal was further irradiated with 635 nm laser at 0.5 W/cm^2 for 3 min after the MN patch was administered for 30 min. To evaluate the efficacy of the treatments for AGA, the animals were subjected to various tests during therapy period. Hair growth was observed and photographed every two days, and the grayscale ratio of the area with new hair covering the treated skin and the hair length were measured on day 15 post-administration.

H&E staining, immunofluorescence, and biochemistry analysis

After the treatment for 15 days, the animals were anesthetized, weighted, and euthanized. Blood samples were collected and analyzed for hematological parameters and serum enzyme levels. The heart, liver, spleen, lung, and kidney were harvested, fixed in 4% paraformaldehyde, embedded in paraffin, sectioned, and stained with hematoxylin and eosin (H&E) for histological examination. Additionally, skin samples were obtained from the depilated area. These skin sample were fixed with formaldehyde (4% w/v), embedded in paraffin, and sectioned into two different patterns. One set of skin tissue slices was cut into 3–4 μm thick sections and stained with H&E for histologicanl evaluation, including HF number, the ratio of terminal hair/vellus hair, and skin thickness. The second set of paraffin sections was used for immunofluorescence evaluations. These sections were incubated with antibodies of anti-β-catenin, anti-Ki67, and anti-CD31. All prepared slides were then examined under a microscope (Olympus FV300, Japan).

Analysis of relative mRNA levels using PCR

To investigate the underlying mechanisms of the indicated formulations on AGA-induced mice, the mRNA expressions of *Srd5a2*, *Ar*, *Dkk1*, *Tgfb1*, *Ctnnb1*, and *Vegfa* in the skin were determined through RT-PCR. 0.1 g of skin sample was homogenized using an Ultra Turrax homogenizer (T18 Basic; IKA) in 1 mL of Trizol reagent. The homogenate was then centrifuged at 4 °C for 15 min at 12, 000 rpm to separate the supernatant containing the mRNA. The mRNA concentration was determined using a NanoDrop 2000 Spectrophotometer (Thermo Scientific, USA). Next, the mRNA was reverse-transcribed into cDNA following the protocols provided by the manufacturer (Accurate Biotechnology Co., Ltd., Hunan, China). The resulting cDNA served as the template for PCR amplification, which was carried out using the Rotor-Gene Q Real-Time PCR cycler (Roche Diagnostics Co., Ltd., Shanghai, China). The primers (Sangon Biotech, Shanghai, China) used for PCR were listed in Table 2.

Table 2 Primer sequence used for quantitative real time PCR on AGA-induced mice

Gene	Forward primer (5′-3′)	Reverse primer (5′-3′)
Gapdh	ATGACCACAGTCCATGCCATC ACT	TGTTGAAGTCGCAGGAGA CAACCT
Srd5a2	TTGGGAAACCCGCCAGTTAC	CATCCCTACCGACACCACAA
Ar	TCCAAGACCTATCGAGGAGCG	GTGGGCTTGAGGAGAACCAT
Dkk1	CTCATCAATTCCAACGCGATCA	GCCCTCATAGAGAACTCCCG
Tgfb1	CCACCTGCAAGACCATCGAC	CTGGCGAGCCTTAGTTTGGAC
Ctnnb1	ATCACTGAGCCTGCCATCTG	GTTGCCACGCCTTCATTCC
Vegfa	TCTTCAAGCCATCCTGTGTG	GCGAGTCTGTGTTTTTGCAG

Statistical analysis

All data are means ± standard deviation (SD), and were analyzed via one- or two-way ANOVAs using SPSS v19 (IBM, USA). $P < 0.05$ was the significance threshold.

Results and discussion

Characterization of BP preparations

SEM analysis revealed prepared BP with clear edges and sizes ranging from 100–250 nm. And the samples displayed clear lattice fringes with the same *d*-spacing of 2.75 Å as the BP crystal (111) (Fig. 2A). As shown in Fig. 2B, BP samples had an average thickness of 5 nm when measured using AFM. These results indicated that we prepared BP with favorable crystallinity and size. Figure 2C shows the XRD patterns for these BP preparations, with diffraction peaks in accordance with standard BP crystal Bragg diffraction peaks (JCPDS Card No.: 74-1878), confirming purity. The Raman spectrum of BP (Fig. 2D) also shows three expected characteristic peaks (A_g^1, B_{2g} and A_g^2).

We modified the BP surface with PEG-NH_2 and then loaded BA through electrostatic reactions. The successful preparation of BP-BA was then demonstrated by a series of characterizations. Firstly, the element distribution in BP-PEG was evaluated via STEM-based EDS mapping

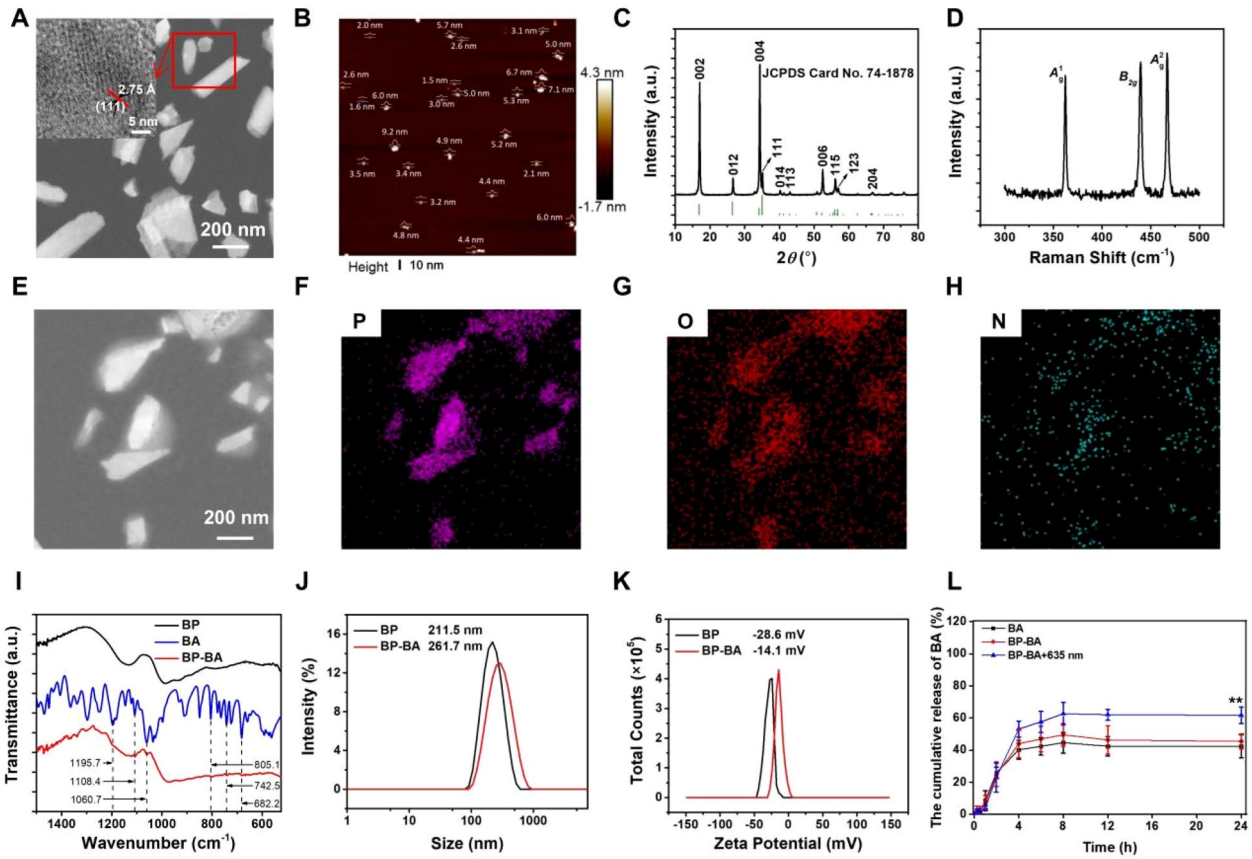

Fig. 2 **A**–**D** SEM image, AFM image, XRD spectrum and Raman spectrum of exfoliated BP, respectively. HRTEM images of BP are inset in (**A**). **E** STEM image of BP-PEG. **F**–**H** P, O and N element mapping from (**E**), respectively. **I** FTIR spectra of BP, BA, and BP-BA. **J**, **K** DLS and zeta potential curves of BP and BP-BA. **L** In vitro release profiles. Data are presented as means ± SD ($n = 6$). $^{**}p < 0.01$ *vs* the BP-BA group

to investigate the success of synthesis (Fig. 2E–H). The STEM bright-field images were surrounded by a darker area, confirming the successful preparation of BP-PEG, which had overlapping N elements. Then, the FTIR spectra of BP, BP-PEG, BA, and BP-BA were shown in Fig. 2I and additional file 1. The BP-BA peak positions were consistent with those of BP (PO_x, 1103 cm^{-1}), BA, confirming that the BP-BA was successfully prepared. We performed ^{1}H NMR analysis for further validation (Additional file 2). ^{1}H NMR analysis revealed that the interactions in BP-BA were mainly through π-π stacking and electrostatic interactions between BA and BP-PEG. DLS analysis showed that BP had an average size of 211.5 nm with a PDI of 0.175. PEG modification reduced size and PDI to 190.3 nm and 0.119, respectively, while BA incorporation increased BP-BA size to 261.7 nm and PDI to 0.176 (Fig. 2J, Additional file 3). The zeta potential value was BP at − 28.6 mV, BP-PEG at − 25.2 mV, and BP-BA at − 14.1 mV (Fig. 2K, Additional file 3). There is a significant reduction in the absolute zeta value of the resultant material due to the addition of BA to BP. The larger particle size of BP-BA than pure BP observed by DLS was therefore attributed to the agglomeration of BP-BA particles with low absolute zeta values. In general, the fabricated BP-BA was subsequently loaded in MNs within one day. we tested the storage stability of the BP-BA and measured the hydrated particle size and PDI in water on days 0, 3 and 5, respectively. As shown in Additional file 4, the particle size of BP-BA after 5 days increased only 14 nm and the PDI increased ~ 0.04 compared to day 0, indicating that BP-BA has good short-term stability.

I*n vitro* release assay demonstrated that 635 nm irradiation (+635 nm) significantly promoted BA release from BP-BA (Fig. 2L), with a 31.40 and 26.37% increase in release within 24 h compared to BA alone and BP-BA without 635 nm laser (BP-BA), respectively. This confirms that light irradiation enhance the drug release [42, 43].

Characterization of photo-thermal performance

We next examined the photo-thermal absorption properties of BP and BP-BA. BP exhibited decreasing absorbance with increasing wavelength (Fig. 3A), and the addition of BA led to a reduction in absorbance (Fig. 3B). This reduction was due to the loss of BP during the preparation of BP-BA and the lower dispersibility of BP-BA compared to pure BP.

To evaluate the repeatability of the thermal behavior induced by 635 nm laser irradiation, BP and BP-BA formulations underwent five consecutive on/off cycles of 5 min laser exposure followed by 5 min of natural cooling (Fig. 3C, D). Both formulations showed an increase in

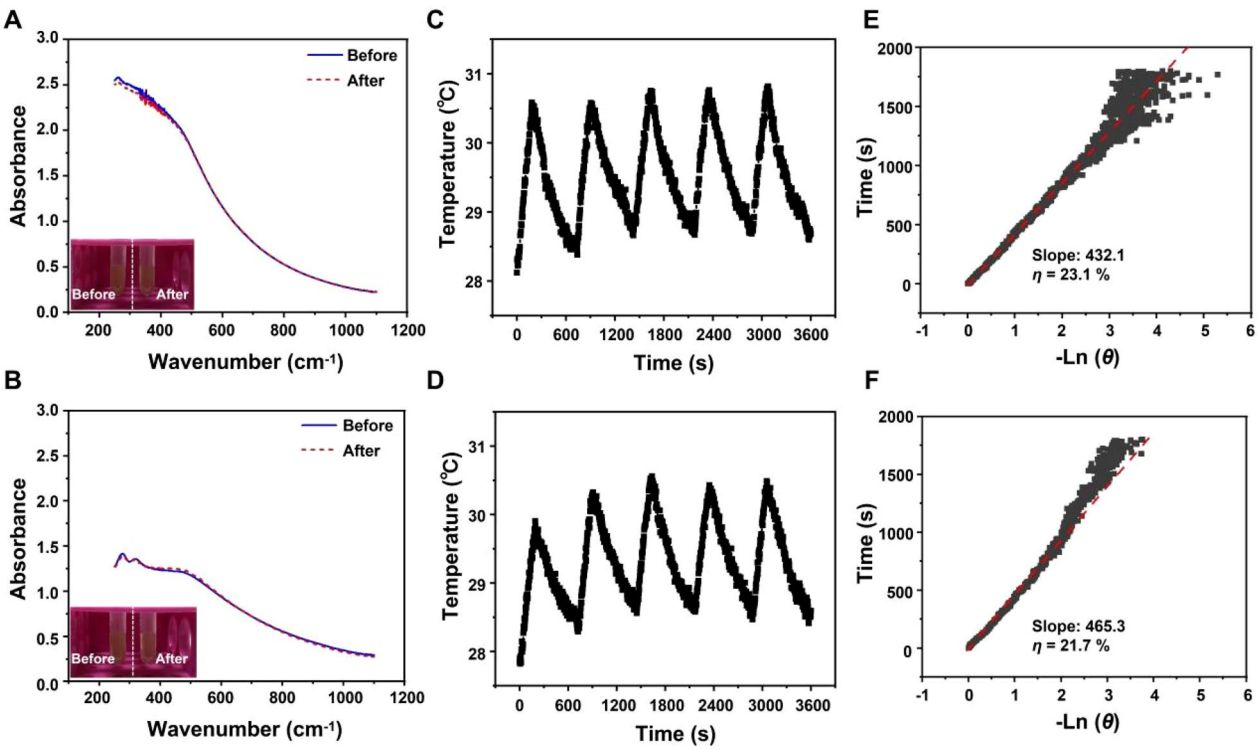

Fig. 3 **A**, **B** Absorbance before and after PT activation for BP and BP-BA, respectively. **C**, **D** PT On/Off cycles for BP and BP-BA, respectively. **E**, **F** Time-[-Ln(θ)] curves for BP and BP-BA, respectively

temperature with time during irradiation, the temperature of BP (Fig. 3C) and BP-BA (Fig. 3D) increased from 27.92 °C and 27.88 °C to 30.57 °C and 30.03 °C after the first irradiation cycle, respectively. Based on the cooling curve yielded after the first PT cycle, the PT conversion efficiency values were calculated to be 23.1 and 21.7% for BP (Fig. 3E) and BP-BA (Fig. 3F), respectively, indicating that the addition of BA slightly reduced the PT conversion efficiency of pure BP.

We further verified whether these preparations possessed heat shielding properties by monitoring the temperature at different locations with 1 mL of large volume of different concentrations of BP or BP-BA subjected to light irradiation (0.5 W/cm^2, 635 nm) for 3 min. As shown in additional file 5, the temperature of high concentration (50 μg/mL) of BP or BP-BA reached a maximum temperature of 32 ℃ during this time period, and the temperature became lower as the detection moved towards the bottom, indicating that the preparations do not produce heat damage to deep skin tissues and have excellent heat shielding properties. Additionally, there was no overheating reaction to the scalp even with large volumes of the preparation solution administered with light irradiation.

I*n vitro* PT performance of BP was also evaluated by irradiating samples of PBS, BP, and BP-BA with a laser irradiation (0.5 W/cm^2, 635 nm) for 3 min. Temperature changes were monitored every 30 s using an IR camera. The results revealed significant PT performance in a time- and concentration-dependent manner (Additional file 6), with both BP and BP-BA showing a rapid and marked temperature increase to approximately 41 °C after just 3 min of 635 nm irradiation. In contrast, the temperature of PBS sample increased only 2 °C after irradiation.

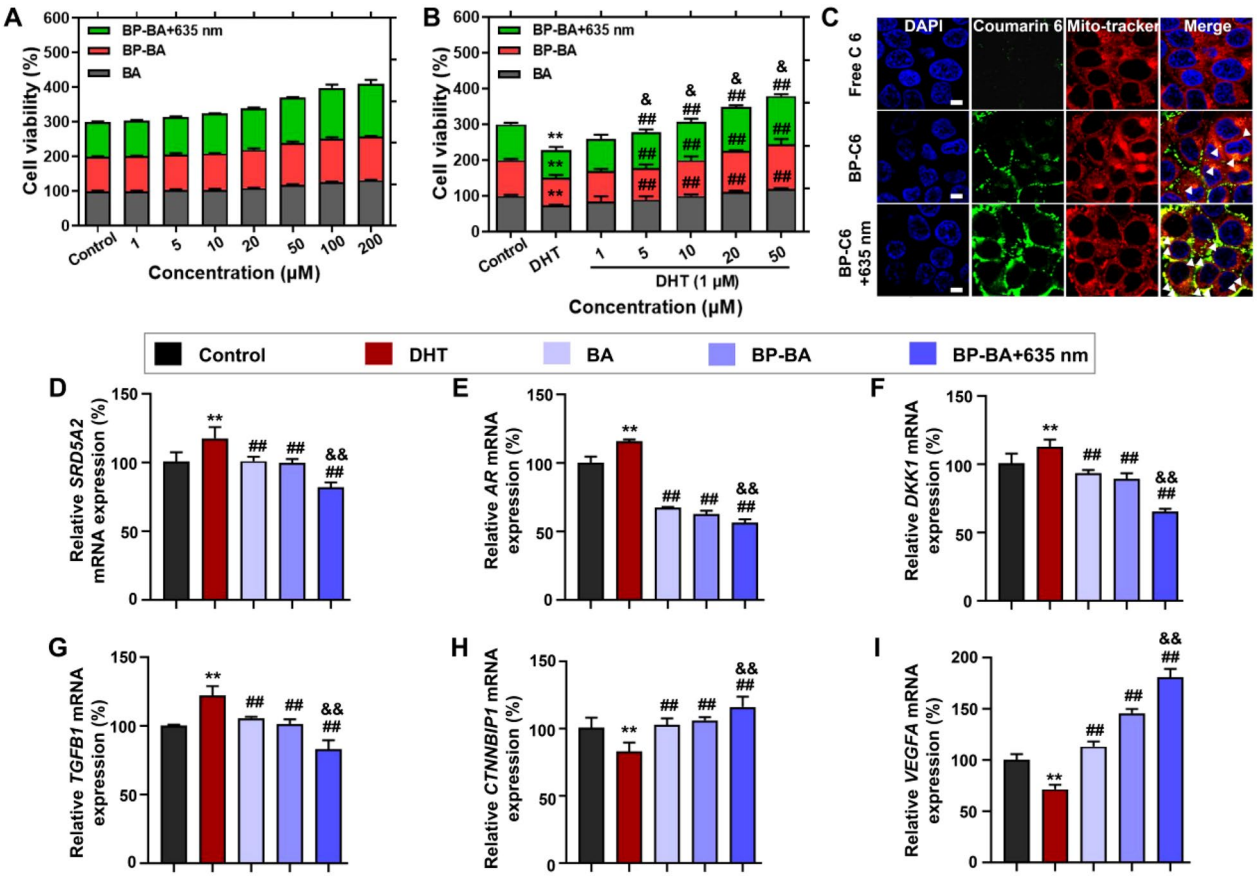

Fig. 4 In vitro biocompatibility analysis and effects on cellular levels in DHT-induced hDPCs. **A** The viability of hDPCs treated with BA, BP-BA, and BP-BA + 635 nm. **B** The indicated treatments were evaluated for their ability to prevent DHT-induced cytotoxicity. **C** Fluorescence co-localization images in mitochondria of different C6-labeled groups, as imaged by CLSM. Scale bar: 5 μm. **D**–**I** The indicated groups regulated mRNA expression levels of DHT-induced hDPCs. They inhibited the mRNA expression of negative genes of *SRD5A2* (**D**), *AR* (**E**), *DKK1* (**F**) and *TGFB1* (**G**), and activated the mRNA expression of positive genes of *CTNNBIP1* (**H**), and *VEGFA* (**I**) in DHT-induced hDPCs. Data are means ± SD (n = 6). $^{**}p < 0.01$ *vs* the Control group. $^{\#\#}p < 0.01$ *vs* the DHT group. $^{\&}p < 0.05$ and $^{\&\&}p < 0.01$ *vs* the BP-BA group

Assessment of in vitro anti-AGA efficacy

The preparations of BA, BP, BP + 635 nm (without BA), BP-BA (without 635 nm laser irradiation), or BP-BA + 635 nm did not show significant cytotoxicity in vitro, and BA or 635 nm irradiation even promoted the proliferation of hDPCs (Fig. 4A and additional file 7). Subsequently, we observed the ability of these preparations to protect hDPs against the DHT induction in vitro [44]. Compared to the control group (the untreated cells), the treatment with 1 μM of DHT reduced the cell viability of hDPCs to approximately 72% (Fig. 4B). When co-incubated with varying concentrations of BA, BP-BA, or BP-BA + 635 nm (containing BA of 1, 5, 10, 20 or 50 μM) for 24 h, there was a dose-dependent increase in cell viability, indicating a protective effect against DHT-induced cell damage. We additionally employed CLSM to visualize the cellular uptake and localization of C6-labeled preparations in hDPCs. Compared to the free C6 group, the fluorescence intensity in cells treated with C6-BP without 635 nm irradiation and C6-BP with 635 nm irradiation (C6-BP + 635 nm) was 2.6 and 4.6 times higher, respectively (Additional file 7). This indicated that BP enhanced C6 cellular uptake and 635 nm irradiation further boosted the uptake. C6 was localized in the mitochondria of the cells (Fig. 4C).

To elucidate the molecular mechanisms of these preparations for anti-AGA, we conducted RT-PCR tests to measure the expression of mRNA levels of various genes in an in vitro DHT-induced AGA cell model. According to Fig. 4D–I, after treatment with DHT, hDPCs exhibited increased mRNA expression of negative regulators such as *SRD5A2*, *AR*, *DKK1*, and *TGFB1*, and decreased expression of positive factors *CTNNBIP1* and *VEGFA* compared to the control group (Fig. 4D–G, and H–I). This suggests that DHT induction has an impact on gene expression, leading to a dysregulation of factors that play a crucial role in hair growth [45]. As expected, treatment with the various preparations significantly reduced the mRNA expression levels of *SRD5A2*, *AR*, *DKK1*, and *TGFB1*, while enhancing those of *CTNNBIP1* and *VEGFA* compared to the DHT-treated group. The abnormal mRNA expressions relative with AGA were normalized by BA formulations, and the amelioration effects was in turn of BP-BA + 635 nm > BP-BA > BA. Interestingly, *VEGFA* expression significantly increased following 635 nm irradiation (BP-BA + 635 nm), to 2.5 times that of the model group. This result highlights that 635 nm irradiation had a significant promoting effect on angiogenesis [46].The mild thermal effects of BP upon 635 nm irradiation presented the promotion effects in the cellular level.

Anti-AGA efficacy in isolated HF organ culture

Mice hair growth ex vivo correlates with hair growth in vivo, although HFs typically begin to regress and cease growth after a few days ex vivo without treatment. We evaluated the effects of various formulations on HF activity in terms of the elongation and maintenance of the growth phase of isolated HFs. Additional file 8 shows the mice vibrissa HF organ culture with different formulations. After a 12 day treatment period, 8 μM of DHT reduced the hair shaft length of vibrissae by about 33% compared to the control treatment. However, subsequent treatments with BA, BP-BA, and BP-BA + 635 nm significantly increased hair shaft length by approximatel 14, 19 and 24%, compared to the DHT group. These results confirm that BA or the mild thermal effect from 635 nm irradiation enhance the HF growth ex vivo, with the combined treatment showing enhanced efficacy in tissue level.

Characterization of BP-BA@MNs

Show Fig. 5A shows the fabrication process of BP-BA@MNs. Brifely, the HA solution containing BP-BA was filled into the MN mold followed by centrifugation to form the MN tips. Subsequently, pure HA solution was added as the backing material, and the fully dried BP-BA@MNs were removed from the mold. BP-BA@MNs were visualized with digital optical microscopy and CLSM. The MNs were arranged in an 12 × 12 array with a length of 800 μm from pedestal to tip on a 10 × 10 mm^2 patch (Fig. 5B). The MN tips displayed a uniform distribution of BP-C6 (C6 mimicked BA for visualization), indicating that BA was evenly distributed in the tip (Fig. 5C). As determined by the texture analyzer, the BP-BA@MNs patch had a mechanical strength of 98.06 ± 0.68 N/patch (Fig. 5D), sufficient to penetrate skin without breaking [47]. Subsequently, to measure the insertion depth of the MNs, we used Parafilm M® as a skin mimic The higher puncture pore ratio allowed the BP-BA@MNs to penetrate Parafilm M® up to the fourth layer (Fig. 5E), indicating an insertion depth of about 400 μm. OCT confirmed that the MNs reached a maximum depth of about 300 μm in isolated rat skin, with no breakage observed during insertion (Fig. 5F). The penetration depth of the BP-BA@MNs was less than 400 μm, this was mainly because of the elasticity of the skin which served as a barrier to the BP-BA@MNs. Methylene blue staining pre- and post-insertion the skin illustrated the MNs' effective porogenic integrity and insertion efficacy, highlighting their potential for transdermal drug delivery (Fig. 5G).

The drug loading of BA in BP-BA@MNs determined with HPLC was 11.68 ± 1.93 μg per patch. The cumulative release rate within 24 h of BA from MNs with or without

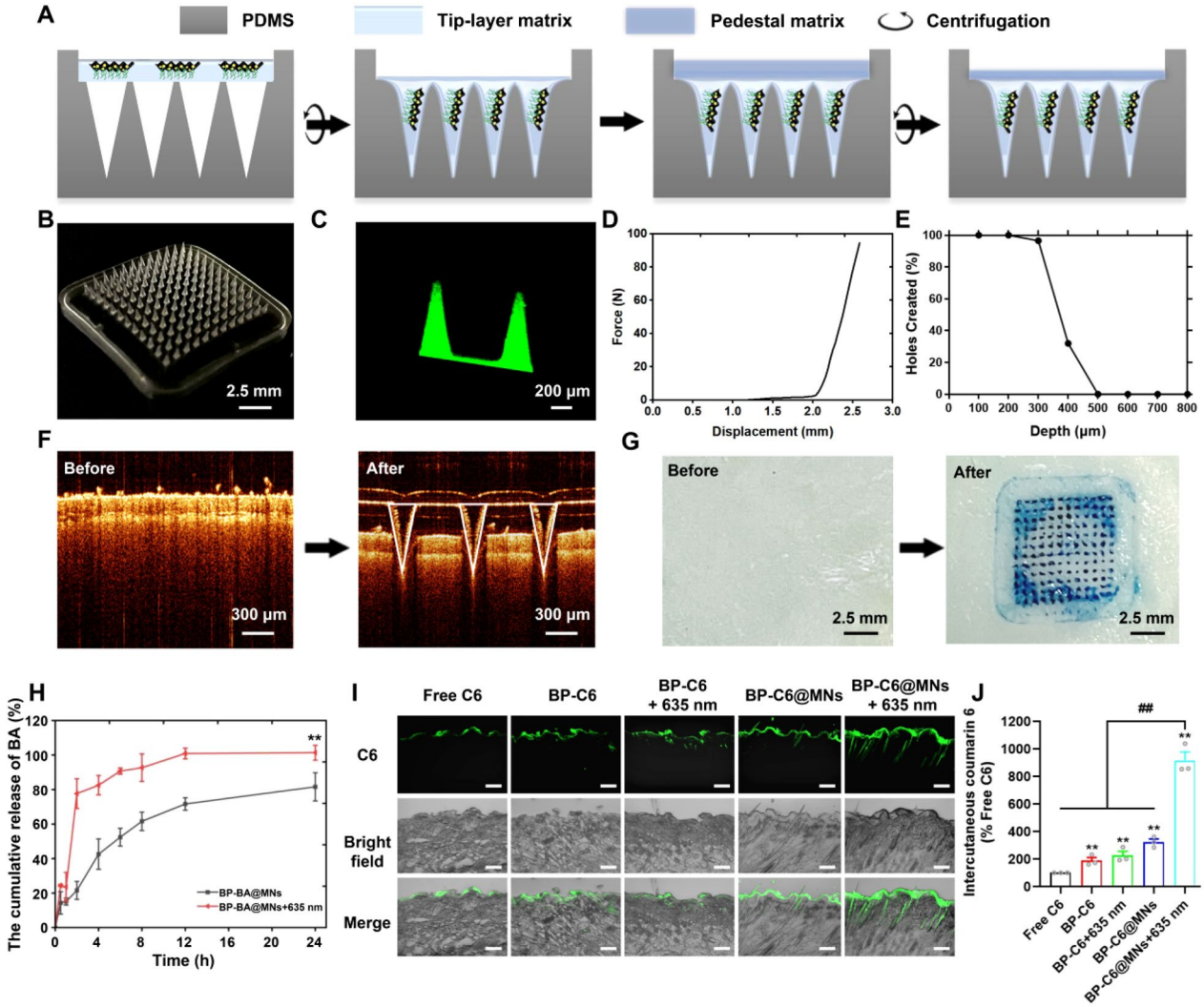

Fig. 5 Fabrication and characterization of BP-BA@MNs. **A** schematic fabrication process of BP-BA@MNs. Photographs of BP-BA@MNs array and needle taken with (**B**) digital microscopy and (**C**) confocal laser scanning microscopy. BP-BA@MNs were characterized by (**D**) mechanical strength and (**E**) insert depth. **F** Images of the optical coherence tomography (OCT) of isolated rat skin before and after BP-BA@MNs application. **G** Photographs of SD rat skin before and after insertion of methylene blue (MB)-BP-BA@MNs. **H** In vitro release profiles. Data are presented as means ± SD ($n = 6$). $^{**}p < 0.01$ *vs* the BP-BA@MNs group. **I** CLSM images of C6 permeation through the rat skin after 4 h treatment with different formulations. Scale bar: 200 μm. **J** Quantitative analysis of intercutaneous C6 fluorescence intensity. Data are means ± SD (n = 3). $^{**}p < 0.01$ *vs* the Free C6 group. $^{\#\#}p < 0.01$ *vs* the BP-BA@MNs + 635 nm group

635 nm irradiation was 100.31 ± 3.33% and 76.18 ± 8.77%, respectively (Fig. 5H), demonstrating that 635 nm laser irradiation significantly enhances the release rate by 24.05%, consistent with our previous in vitro *release* findings of BP-BA + 635 nm.

The storage stability of BP-BA@MNs was evaluated in terms of the mechanical strength, insertion depth, and BA content of BP-BA@MNs at 0, 7, and 14 days, respectively (additional file 9). The results showed that compared with day 0, the mechanical strength of BP-BA@MNs remained above 90 N after 14 days, and there was no significant changes in the insertion depth and the content of BA in BP-BA@MNs. Therefore, BP-BA@MNs have good storage stability. However, the long-storage test of BP-BA@MN is being investigated.

Measurement of HF permeability in vivo

The skin is primarily composed of three layers: epidermis, dermis, and subcutaneous tissue. The epidermal layer is further divided into the stratum corneum (SC) and the viable epidermis. The thickness of the SC, viable epidermis, and dermis is 10–20 μm, 100–150 μm, and

3–5 mm, respectively [48]. HFs, as skin appendages, are anchored in the skin of dermis, targeted HF delivery system is anticipated to deliver drugs to dermis.

To assess the efficiency of the preparations in targeting HFs and transdermal penetration in vivo, we topically applied C6, BP-C6, BP-C6 + 635 nm, BP-C6@MNs or BP-C6@MNs + 635 nm on mice. CLSM was used to analyze cryosections of dorsal skin following these applications. As shown in Fig. 5I and J, after 4 h of treatments, C6 from the C6 suspension predominantly accumulated in the SC, specifically within the depth of 10–20 μm. While C6 from BP-C6 predominantly concentrated in the SC and slightly permeated into the viable epidermis, reaching the depth of ~ 40 μm. This indicated that C6 was difficult to effectively penetrate the skin when a single loading system was utilized [49]. After irradiated with 635 nm laser, the C6 permeated into deeper viable epidermis at the depth of ~ 100 μm. The irradiation with 635 nm laser enhanced the drug penetration due to the PT effect. The BP-C6@MNs delivered C6 at the depth of ~ 180 μm. Furthermore, BP-C6@MNs under 635 nm irradiation (BP-C6@MNs + 635 nm) resulted in a significant enhancement in permeation depth of C6, reaching approximately 350 μm in the dermis, and the C6 fluorescence was observed along the HF. This suggested that MNs are highly effective in targeted drug delivery to follicular structures. Besides, it has been reported that HA as the MN materials exhibits a better affinity for HF-related structures [50]. Quantitative fluorescence analysis revealed that BP-C6@MNs + 635 nm was 4.04-fold and 2.84-fold to BP-C6 + 635 nm and to BP-C6@MNs, respectively (Fig. 5J). These results provide an evidence that the combination of PT and MNs is a highly effective method for delivering drugs to the skin [51]. PT-assisted drug delivery could be a promising approach for treating a wide range of skin conditions, offering an effective way to deliver drugs to the skin and accumulate in the HF site.

Hair growth efficiency in the AGA model

The PT efficacy of BP-BA or BP-BA@MNs was evaluated in vivo. Using a thermal camera, we monitored the temperature changes (ΔT) of animal skin under 635 nm laser irradiation at a power density of 0.5 W/cm2 for 3 min (Additional file 10). The animals treated with PBS showed a minimal ΔT of 1.7 °C. In contrast, those treated with BP-BA or BP-BA@MNs exhibited a much higher change in temperature, up to 14.4 °C and 14.3 °C, respectively. Consequently, mice subjected to these treatments attained final dorsal temperatures of 41.3 °C and 41.9 °C, aligning with with the requirements for in vivo mild photothermal therapy [52]. The PT efficacy was consistent with the results of in vitro experiments.

To further investigate the effects of these preparations on hair growth, an AGA model was induced by testosterone. Additional file 11 shows a schematic diagram of the AGA modeling and treatment. Throughout the 15 days' treatment, formulations containing MNs were applied every three days, whereas other treatments were applied daily. Figure 6A and Additional file 12 show the representative and all (n = 6) dorsal skin photographs of the hair re-growth process from day 0 to day 15 after treatment. Hair growth was visually documented and quantitatively scored throughout this period. Notably, the BP-BA@MNs + 635 nm treatment had significantly higher hair growth scores compared to the other groups, although slightly lower than the control and MXD group (Fig. 6B). After 15 days' treatment, hair coverage area demonstrated that BP-BA@MNs + 635 nm treatment was the most effective in promoting hair growth, achieving 93.63% hair regrowth (Fig. 6C). In comparison, the BP-BA + 635 nm group and BP-BA@MNs group only resulted in 56.98 and 57.77% of hair regeneration, respectively. The average hair length of the mice in the BP-BA@MNs + 635 nm group was longer than that the other group (Fig. 6D). Together, the enhanced efficacy of the BP-BA@MNs + 635 nm highlights the synergistic effect of MNs and PT in promoting hair regeneration in an AGA model, even with reduced frequency of application.

H&E staining for hair regrowth evaluation

Histological analysis using H&E staining of dorsal skin after 15 days of treatment confirmed the promotion of hair regrowth (Fig. 6E–I). AGA is characterized with thinned skin, smaller dermal papillae, and fewer HF due to inadequate blood supply. This pathology often leads to the upward migration and gradual miniaturization of HFs, resulting in the replacement of terminal hairs with vellus hairs [53]. As shown in Fig. 6E, the model

(See figure on next page.)

Fig. 6 Evaluation of the pharmacodynamics in vivo. **A** Representative photographs of hair growth on the dorsal skin on day 0, 3, 6, 9, 12, and 15. **B** Quantitative distributions of hair growth score of the dorsal skin of mouse treated with different formulations during days 0–15. The corresponding skin color grayscale ratio (**C**) and hair length (**D**) on day 15 post-treatment. Data are means ± SD (n = 6). H&E staining of hair follicle regeneration on the longitudinal (**E**) and transverse (**G**) mouse dorsal skin. **F** Quantitative analysis of skin thickness on day 15 post-treatment. Quantitative analysis of (**H**) the number of hair follicle and (**I**) the ratio of terminal hair/vellus hair. Data are means ± SD (n = 3). $^{**}p < 0.01$ *vs* the Control group. $^{\#\#}p < 0.01$ *vs* the Model group. $^{\&\&}p < 0.01$ *vs* the BP-BA@MNs group

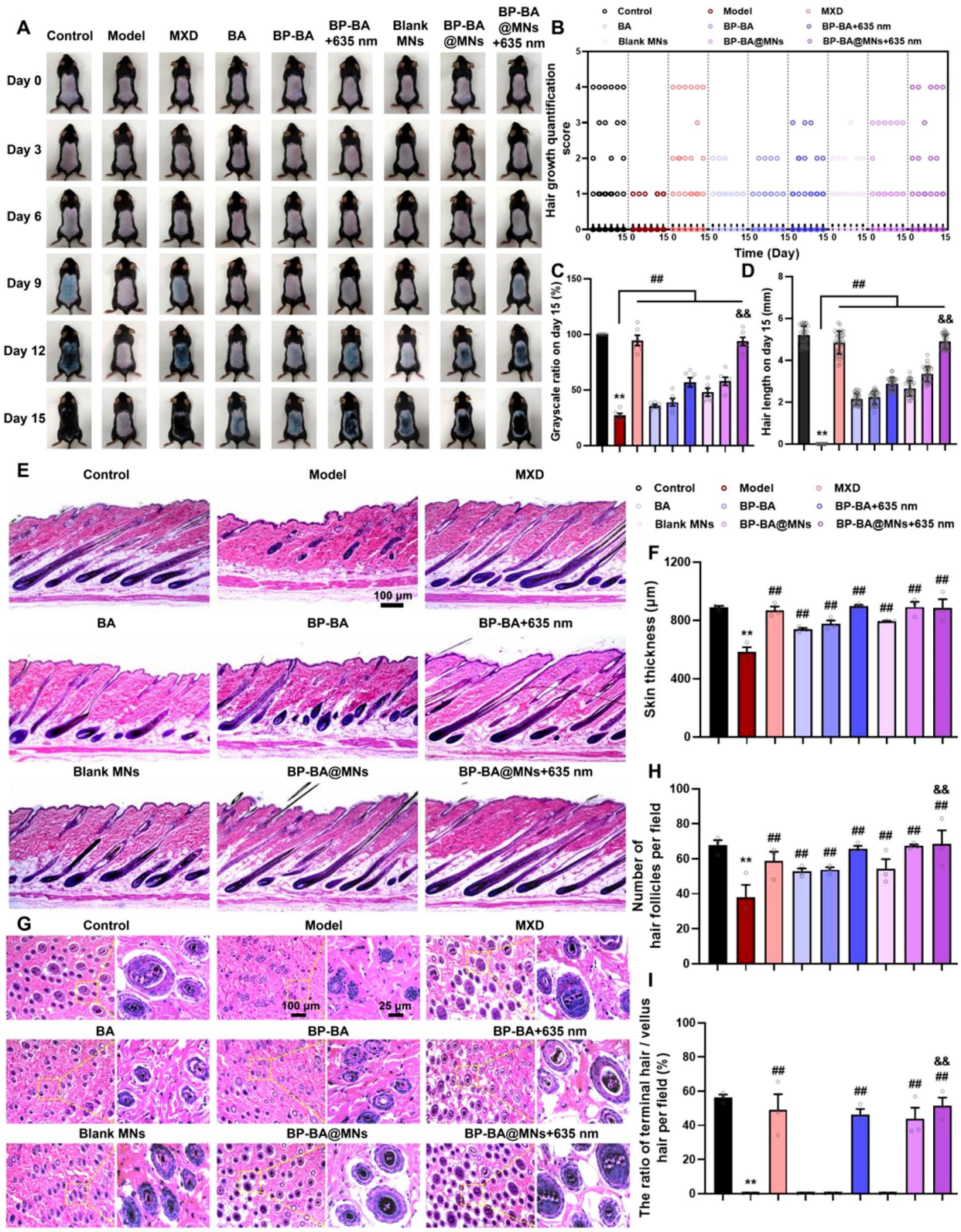

Fig. 6 (See legend on previous page.)

group exhibited significant skin thinning, minimal dermal papillae, and miniaturized HFs. In contrast, mice treated with different formulations displayed increased skin thickness and enlarged hair bulbs, characteristics associated with the mid-late anagen phase of hair growth, clearly delineating the differences in hair density and morphology between treated groups and the model group (Fig. 6E). Notably, the testosterone-induced model group showed a 34.43% reduction in skin thickness compared to the control group (Fig. 6F). At the same time, the mice treated with blank MNs, BP-BA@MNs, and BP-BA@MNs + 635 nm showed no irreversible skin damage on the 15th day post-treatment, indicating that transdermal administration of MNs is safe.

HFs pass through three distinct stages during their life cycle: rest (telogen), growth (anagen) and regression (catagen) [54]. During the anagen phase, the number and size of HF increase. Normally, the scalp produces more terminal hairs than vellus hairs. However, in our AGA model induced by testosterone, both the volume and number of HF decreased, altering the ratio of terminal to vellus hairs with an increase in vellus hairs. Concurrently, the hair shaft underwent a reduction in both the number and the diameter (Fig. 6G). Treatment with various formulations significantly increased the number of HFs and improved the ratio of terminal to vellus hairs, demonstrating the effectiveness of the treatments in reversing testosterone-induced changes (Fig. 6H and I). The ratio of terminal to vellus hairs for the different groups was as follows: MXD group (49.10 ± 15.78%), BP-BA + 635 nm group (46.22 ± 5.82%), BP-BA@MNs group (43.68 ± 11.38%), and BP-BA@MNs + 635 nm group (51.46 ± 8.27%).

Immunofluorescence staining for hair regrowth evaluation

The Wnt/β-catenin signaling pathway plays a significant role in the hair cycle, acting as the key driving force in the transition from telogen to anagen [55]. Abnormal regulation of this pathway can lead to hair growth disorders, which affects the size and shape of HF. The expression of β-catenin was analyzed via immunofluorescence staining. In the testosterone-induced model group, β-catenin expression significantly decreased and was primarily localized in the upper region of the HFs. Conversely, treatment with BP-BA@MNs + 635 nm markedly increased β-catenin expression, concentrating it in the lower part of the HF, within the outer and inner root sheath (Fig. 7A and B). This suggests that the treatment with BP-BA@MNs + 635 nm facilitates the transition of HF growth cycle. Additionally, areas treated with the preparations showed higher levels of Ki67, a marker of cell proliferation, consistent with anagen phase induction Fig. 7C and D). The expression levels of Ki67 in the MXD group, BP-BA + 635 nm group, BP-BA@MNs group, and BP-BA@MNs + 635 nm group were 3.20, 2.70, 2.59, and 3.48-fold to that of the model group, respectively.

Additionally, the angiogenesis of capillaries and perifollicular vessels were also examined. Immunofluorescence staining of CD31 in mice dorsal skin revealed increased blood vessel formation in alopecia areas treated with the indicated preparations compared to the model group (Fig. 7C). This increase could be attributed to: 1) BA has been reported to have a beneficial effect on promoting angiogenesis [56]; 2) 635 nm irradiation promotes angiogenesis by increasing the permeability of the perivascular space, thereby increasing blood flow [57]; 3) MNs stimulate angiogenesis through mechanical stimulation [35]. Remarkably, CD31 expression in BP-BA@MNs + 635 nm group was four times higher than that of the model group, comparable to that daily topical application of commercial MXD group, despite the fact that the BP-BA@MNs + 635 nm was administered every three days during the treatment period for only five applications (Fig. 7E). Thus, the molecular mechanisms underlying these observed effects will be elucidated in the further experiments.

Determination of HF-related mRNA expression in AGA

Hair regrowth is highly regulated by various factors involved in the HF cycle, whose inhibition or activation affects hair growth. Based on in vitro cellular experiments, we have confirmed that both BA and 635 nm irradiation effectively regulate hair growth-related factors. To elucidate the molecule mechanisms by which the indicated preparation groups restored or promoted hair growth, we analyzed the changes in the same signaling molecules as the in vivo experiments (Fig. 8). AGA is closely associated with the expression of *Srd5a2*, an enzyme critical for converting testosterone into DHT, a potent androgen with a very high affinity tor *Ar* [58, 59]. Elevated levels of *Srd5a2* and *Ar* are known primary drivers of AGA. In our study, the model group significantly increased *Srd5a2* and *Ar* mRNA expressions by 2.02-fold and 2.46-fold, respectively. In comparison to the model group, the MXD group, the BP-BA + 635 nm group, the BP-BA@MNs group, and the BP-BA@MNs + 635 nm group markedly reduced mRNA expressions of *Ar* by 10.16, 39.15, 40.61, and 47.69%, respectively and *Srd5a2* by 42.25, 33.16, 33.62, and 38.21%, respectively (Fig. 8A and B). More importantly, the BP-BA@MNs + 635 nm treatment reduced *Ar* mRNA expression more than 1.71-fold compared to the MXD group. Molecular docking simulation supported this finding by displaying BA's strong binding affinity to *Ar* and *Srd5a2*, providing a theoretical basis for its efficacy in targeting the two major pathological factors of AGA (Additional file 13).

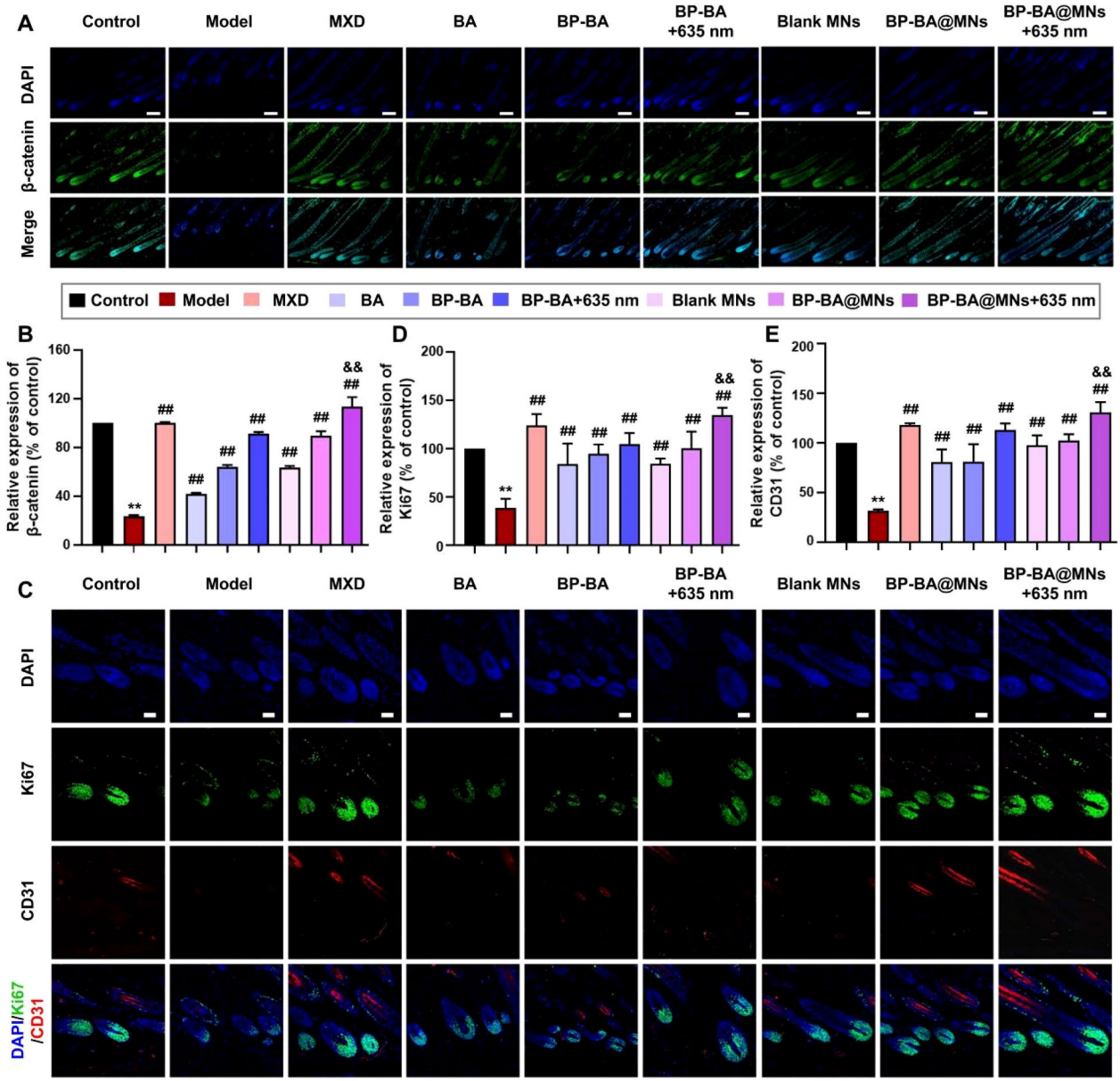

Fig. 7 **A** Representative images of β-catenin immunofluorescence staining on depilated skin on day 15 post-treatment. Scale bar: 100 μm. Images represent at the HF site. **B** Quantification of the relative expression of β-catenin on the mice dorsal skin treated with different groups. Data are means ± SD (n = 3). **C** Representative images of immunofluorescence staining of Ki67 and CD31 on depilated skin on day 15 to investigate the expression of proliferation markers and perifollicular angiogenesis. Scale bar: 50 μm. Images represent at the HF site. Quantification of the relative expression of (**D**) ki67 and (**E**) CD31 on the mice dorsal skin treated with different formulations. Data are means ± SD (n = 3). $^{**}p < 0.01$ *vs* the Control group. $^{\#\#}p < 0.01$ *vs* the Model group. $^{\&\&}p < 0.01$ *vs* the BP-BA + 635 nm group or the BP-BA@MNs group

As mentioned previously, β-catenin promotes the induction and duration of the HF anagen phase, while Dkk1, a potent antagonist of the Wnt/β-catenin signaling pathway, drives the catagen phase and apoptotic cell death in HFs [60, 61]. Similarly, *Tgfb1* is a recognized promoter of the catagen phase [62]. In this context, our results showed that testosterone induction significantly decreased *Ctnnb*1 expression while increasing *Dkk1* and *Tgfb1* expressions (Fig. 8C–E). The treatment with BP-BA@MNs + 635 nm significantly reversed these effects, elevating Ctnnb1 expression by 78.52% and reducing Dkk1 and Tgfb1 expressions by 71.47% and 65.49%, respectively, outcomes that not only improved

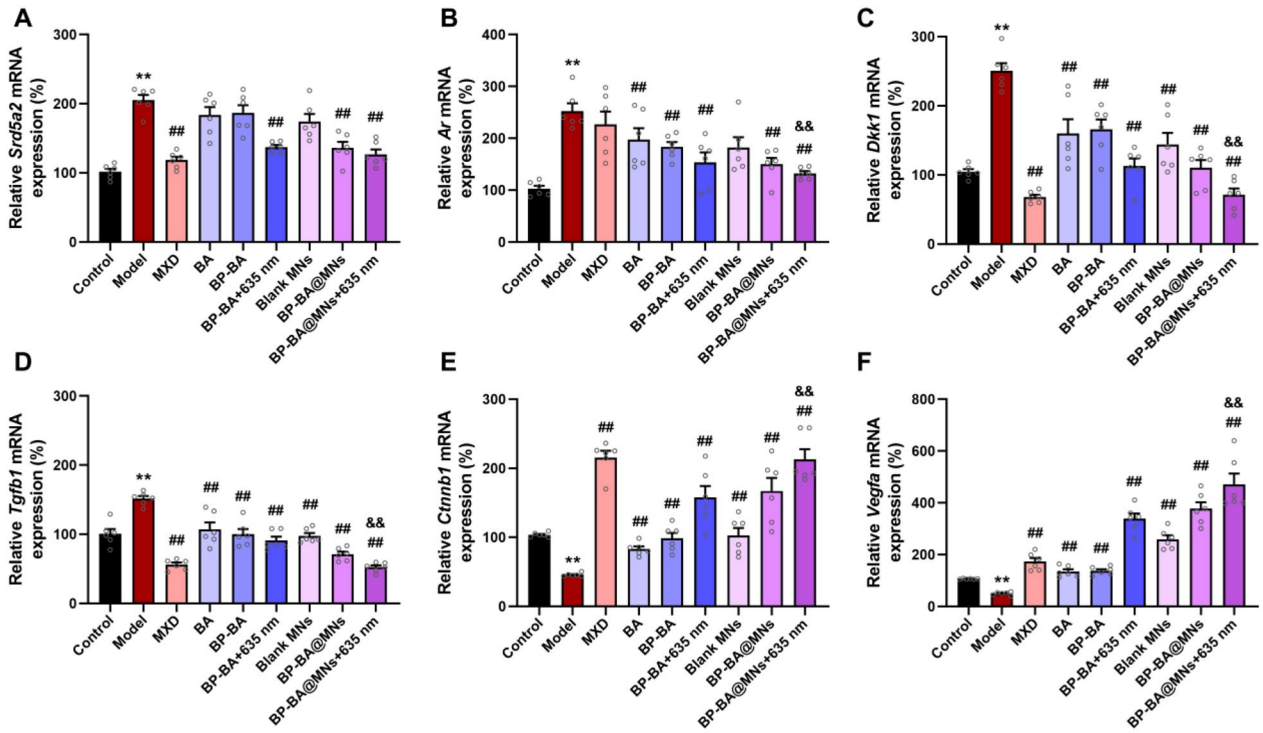

Fig. 8 The mRNA expression levels in the dorsal skin of the AGA mice treated with different formulations. They inhibited the mRNA expression of negative genes of *Srd5a2* (**A**), *Ar* (**B**), *Dkk1* (**C**) and *Tgfb1* (**D**), and activated the mRNA expression of positive genes of *Ctnnb1* (**E**), and *Vegfa* (**F**). Data are means ± SD (n = 6). $^{**}p < 0.01$ *vs* the Control group. $^{\#\#}p < 0.01$ *vs* the Model group. $^{\&\&}p < 0.01$ vs the BP-BA + 635 nm group or the BP-BA@MNs group

upon other treatment groups but were also comparable to the MXD group.

VEGF, a biomarker of angiogenesis and a key growth factor for hair growth, was shown to have a good pro-angiogenic effect from the immunofluorescence results in the indicated preparation groups. Here we further evaluated the effect of different formulations on the expression of *Vegfa* mRNA at the molecular level (Fig. 8F). The results showed that *Vegfa* mRNA was significantly more expressed in the alopecia areas treated with the above indicated preparation groups compared to the model group, consistent with CD31 staining results. Remarkably, even a single mode of therapy in the preparation groups promoted a high level of *Vegfa* mRNA expression, thus supporting our interpretation of high CD31 expression.

In summary, testosterone induction disrupts normal HF growth by altering the expression of crucial genes. Our BP-BA@MNs + 635 nm treatment effectively counteracted these changes, offering a targeted therapeutic approach to AGA by normalizing gene expression related to HF cycling and growth.

In vivo biocompatibility evaluation

After a 15-day treatment, we collected blood samples from the animals and analyzed them for hematological parameters and serum enzyme levels. The results were documented in Additional file 14. There were no significant differences across the various groups, indicating that the treatments did not cause significant hepatic and renal toxicity. Further analysis of major organs using H&E staining revealed no significant tissue damage, and there was also no observed weight loss in the treated mice. These findings affirm that the treatments possess good histocompatibility, suggesting their safety for prolonged use.

Conclusions

In summary, we developed a novel transdermal drug delivery strategy that combines MNs with BP-based mild photothermal effects for the treatment of AGA. Utilizing the mild photothermal effects of BP to enhance the transdermal drug delivery via MNs, this system significantly improved the intracutaneous transport of BA, achieving a synergistic efficacy in the treatment of AGA. The BP-BA

effectively promoted the proliferation of hDPCs in vitro, and regulated the multiple abnormal gene expressions related to HF-growth. In a testosterone-induced AGA animal model, the combination of MNs with the photothermal effects of BP-BA led to a considerably faster hair regrowth, at a lower dosing frequency than traditional treatments. This innovative approach not only normalized the HF environment affected by androgen damage but also stimulated perifollicular angiogenesis without causing irreversible damage to the skin. Importantly, no obvious side effects or toxicity were observed in the major organs or blood post-treatment. BP-BA@MNs is a promising multifunctional strategy for treating AGA.

Abbreviations

AGA	Androgenic alopecia
AR	Androgen receptors
AFM	Atomic force microscopy
BA	Baicalin
BP	Black phosphorus nanosheets
BP-BA	BP modified PEG loaded BA
BP-BA@MNs	Microneedle patches coated with BP-BA foumulations
Blank-MNs	Microneedle patches without contain BP-BA
CTNNBIP1	Beta-catenin
CLSM	Confocal laser scanning microscope
DKK1	Dickkopf-related protein 1
DHT	Dihydrotestosterone
DLS	Dynamic light scattering
FTIR	Fourier transform infrared spectroscopy
HF	Hair follicle
hDPCs	Human dermal papilla cells
MXD	Minoxidil
MN	Microneedle
NMP	N-methyl-2-pyrrolidone
OCT	Optical coherence tomography
PT	Photo thermal
PDI	Polydimethylsiloxane
SC	Stratum corneum
SRD5A2	5α-Reductase
TGFB1	Transforming growth factor beta 1
TEM	Transmission electron microscopy
VEGFA	Vascular endothelial growth factor
XRD	X-ray diffraction

Supplementary Information

The online version contains supplementary material available at https://doi.org/10.1186/s12951-025-03242-z.

Additional file 1. Characterization of BP-PEG. Fig. S1. FTIR spectra.

Additional file 2. Fig. S2. ^{1}H-nuclear magnetic resonance spectra of BP-PEG, BA, and BP-BA.

Additional file 3. Fig. S3. DLS curves. Fig. S4. Zeta potential curves of PEG, BA and BP-PEG.

Additional file 4. Fig. S5. The stability trials for BP-BA.

Additional file 5. Fig. S6. *In vitro* temperature curves of BP and BP-BA at different concentrations and positions.

Additional file 6. Measurement of PT performance. Fig. S7. The photothermal effect of BP at different concentrations. Fig. S8. Infrared images of PBS, BP, and BP-BA were captured at multiple time points.

Additional file 7. Fig. S9. The cell viability of hDPCs treated with BP or BP combined with 635 nm irradiation was assessed. Fig. S10. Quantitative analysis of cellular internalized C6 fluorescence intensity.

Additional file 8. Fig. S11. Analysis of the effects of *in vitro* isolated hair follicle organ culture.

Additional file 9. Fig. S12. The stability tests for BP-BA@MNs.

Additional file 10. Fig. S13.Thermal images of mice exposed to 635 nm laser irradiation following the indicated groups.

Additional file 11. Fig. S14. Schematic diagram of the experimental protocol.

Additional file 12. Fig. S15. Overall photos of hair growth in the AGA model.

Additional file 13. Molecular dynamics simulation. Fig. S16. Molecular dynamics simulation of BA and bicalutamide (as a positive drug) binding to the androgen receptor. Fig. S17. Molecular dynamics simulation of BA and finasteride (as a positive drug) binding to the 5α-reductase.

Additional file 14. *In vivo* biocompatibility evaluation. Fig. S18. Blood panel analysis and serum biochemistry assay of mice treated with different groups. Fig. S19. H&E staining of heart, liver, spleen, lung, and kidney tissue sections from animals in the indicated treatment groups. Fig. S20. Body weight of treated mice were monitored.

Acknowledgements
Not applicable.

Author contributions
S. X and Z. L contributed equally to this work, and all authors contributed significantly to this work. S. X. performed the methodology, software, data curation, and writing-original draft preparation. Z. L performed the methodology, software, data curation,writing-original draft preparation, and funding acquisition. S. J performed the methodology and validation.T. X performed the investigation and validation. Y. W performed the methodology and validation. C. C performed the methodology and validation. S. G performed the software, data curation, and investigation. X. L perfomred the investigation and validation. Z. P performed the investigation and validation. J. L performed the investigation and validation.Y. X performed the conceptualization, supervision,resources, writing- reviewing and editing, and funding acquisition. All authors reviewed and approved the final manuscript.

Funding
The work was financially supported by National Natural Science Foundation of China, China (No. 82274109 and No. 81973491) and the Guangdong Basic and Applied Basic Research Foundation (2022A1515010428), Research Fund of Guangdong-Hong Kong-Macao Joint Laboratory for Intelligent Micro-Nano Optoelectronic Technology (2020B1212030010) and Macau University of Science and Technology Faculty Research Grants (FRG-23-015-FIE).

Availability of data and materials
Data will be made available on request.

Declarations

Ethics approval and consent to participate
The animal experiments were conducted following Sun Yat-sen University guidelines for animal research and use. The approved ethical protocol number is SYSU-IACUC-2021-B1284.

Competing interests
The authors declare no competing interests.

Consent for publication
All authors agreed to submit this manuscript.

Received: 5 October 2024 Accepted: 18 February 2025
Published online: 27 February 2025

References

1. Lolli F, Pallotti F, Rossi A, Fortuna MC, Caro G, Lenzi A, Sansone A, Lombardo F. Androgenetic alopecia: a review. Endocrine. 2017;57:9–17. https://doi.org/10.1007/s12020-017-1280-y.
2. Padule K, Shinde S, Chitlange S, Giram P, Nagore D. The advancement of herbal-based nanomedicine for hair. Cosmetics. 2022;9:118–50. https://doi.org/10.3390/cosmetics9060118.
3. Mishra P, Handa M, Ujjwal RR, Singh V, Kesharwani P, Shukla R. Potential of nanoparticulate based delivery systems for effective management of alopecia. Colloid Surf B Biointerfac. 2021;208:112050–66. https://doi.org/10.1016/j.colsurfb.2021.112050.
4. Devjani S, Ezemma O, Kelley KJ, Stratton E, Senna M. Androgenetic alopecia: therapy update. Drugs. 2023;83:701–15. https://doi.org/10.1007/s40265-023-01880-x.
5. Li C, Pan L, Yang L, Kong J, Zhang L. An umbrella review of the use of platelet-rich plasma in the treatment of androgenetic alopecia. J Cosmet Dermatol. 2023;22:1463–76. https://doi.org/10.1111/jocd.15617.
6. Kaiser M, Abdin R, Gaumond SI, Issa NT, Jimenez JJ. Treatment of androgenetic alopecia: current guidance and unmet needs. Clin Cosmet Invest Dermatol. 2023;16:1387–406. https://doi.org/10.2147/ccid.s385861.
7. Gasmi A, Mujawdiya PK, Beley N, Shanaida M, Lysiuk R, Lenchyk L, Noor S, Muhammad A, Strus O, Piscopo S. Natural compounds used for treating hair loss. Curr Pharm Design. 2023;29:1231–44. https://doi.org/10.2174/1381612829666230505100147.
8. Nestor MS, Ablon G, Gade A, Han H, Fischer DL. Treatment options for androgenetic alopecia: efficacy, side effects, compliance, financial considerations, and ethics. J Cosmet Dermatol. 2021;20:3759–81. https://doi.org/10.1111/jocd.14537.
9. Wang L, Xian YF, Loo SKF, Ip SP, Yang W, Chan WY, Lin ZX, Wu JCY. Baicalin ameliorates 2,4-dinitrochlorobenzene-induced atopic dermatitis-like skin lesions in mice through modulating skin barrier function, gut microbiota and JAK/STAT pathway. Bioorg Chem. 2022;119:105538–54. https://doi.org/10.1016/j.bioorg.2021.105538.
10. Xing F, Yi WJ, Miao F, Su MY, Lei TC. Baicalin increases hair follicle development by increasing canonical Wnt/-catenin signaling and activating dermal papillar cells in mice. Int J Mol Med. 2018;41:2079–85. https://doi.org/10.3892/ijmm.2018.3391.
11. Chen L, Fan B, Gu H, Yang L, Li X. Effects of baicalin on alopecia and the associated mechanism. Biomed Res Int. 2022;2022:3139123–36. https://doi.org/10.1155/2022/3139123.
12. Jin BR, An HJ. Baicalin alleviates benign prostate hyperplasia through androgen-dependent apoptosis. Aging. 2020;12:2142–55. https://doi.org/10.18632/aging.102731.
13. Jakab G, Bogdan D, Mazak K, Deme R, Mucsi Z, Mandity IM, Noszal B, Kallai-Szabo N, Antal I. Physicochemical profiling of baicalin along with the development and characterization of cyclodextrin inclusion complexes. AAPS PharmSciTech. 2019;20:314–26. https://doi.org/10.1208/s12249-019-1525-6.
14. Mir-Palomo S, Nacher A, Ofelia Vila-Buso MA, Caddeo C, Letizia Manca M, Ruiz Sauri A, Escribano-Ferrer E, Manconi M, Diez-Sales O. Co-loading of finasteride and baicalin in phospholipid vesicles tailored for the treatment of hair disorders. Nanoscale. 2020;12:16143–52. https://doi.org/10.1039/d0nr03357j.
15. Zeng Q, Wang Z, Zhu Z, Hu Y, Wang Y, Xue Y, Wu Y, Guo Y, Liang P, Chen H. Glycyrrhizin micellar nanocarriers for topical delivery of baicalin to the hair follicles: a targeted approach tailored for alopecia treatment. Int J Pharm. 2022;625:122109–22. https://doi.org/10.1016/j.ijpharm.2022.122109.
16. Zhang X, Zhang W. Synthesis of black phosphorus and its applications. Mater Today Phys. 2024;43:101396–419. https://doi.org/10.1016/j.mtphys.2024.101396.
17. Zhou Q, Chen Q, Tong Y, Wang J. Light-induced ambient degradation of few-layer black phosphorus: mechanism and protection. Angew Chem Int Ed Engl. 2016;55:11437–41. https://doi.org/10.1002/anie.201605168.
18. Lan Z, Liu WJ, Yin WW, Yang SR, Cui H, Zou KL, Cheng GW, Chen H, Han YH, Rao L. Biomimetic MDSCs membrane coated black phosphorus nanosheets system for photothermal therapy/photodynamic therapy synergized chemotherapy of cancer. J Nanobiotechnol. 2024;22:174–90. https://doi.org/10.1186/s12951-024-02417-4.
19. Zhou J, Li T, Zhang M, Han B, Xia T, Ni S, Liu Z, Chen Z, Tian X. Thermosensitive black phosphorus hydrogel loaded with silver sulfadiazine promotes skin wound healing. J Nanobiotechnol. 2023;21:330–48. https://doi.org/10.1186/s12951-023-02054-3.
20. Lee G, Choi W, Kim C, Hahn SK, Lee JH. Hyaluronate-black phosphorus-upconversion nanoparticle complex for non-invasive theranosis of skin cancer. Biomacromol. 2022;23:3602–11. https://doi.org/10.1021/acs.biomac.2c00506.
21. Zhang W, Zhang X, Ono LK, Qi Y, Oughaddou H. Recent advances in phosphorene: structure, synthesis, and properties. Small. 2023;20:e2303115. https://doi.org/10.1002/smll.202303115.
22. Lama SBC, Pérez-González LA, Kosoglu MA, Dennis R, Ortega-Quijano D. Physical treatments and therapies for androgenetic alopecia. J Clin Med. 2024;13:4534–52. https://doi.org/10.3390/jcm13154534.
23. Saceda-Corralo D, Dominguez-Santas M, Vano-Galvan S, Grimalt R. What's new in therapy for male androgenetic alopecia? Am J Clin Dermatol. 2023;24:15–24. https://doi.org/10.1007/s40257-022-00730-y.
24. Wang R, Jiang G, Aharodnikau UE, Yunusov K, Sun Y, Liu T, Solomevich SO. Recent advances in polymer microneedles for drug transdermal delivery: design strategies and applications. Macromol Rapid Commu. 2022;43:2200037–56. https://doi.org/10.3390/polym13152405.
25. Wipf A, Boysen N, Hordinsky MK, Dando EE, Sadick N, Farah RS. The rise of transcutaneous drug delivery for the management of alopecia: a review of existing literature and an eye towards the future. J Cosmet Laser Ther. 2019;21:247–54. https://doi.org/10.1080/14764172.2018.1525743.
26. Nguyen HX, Nguyen CN. Microneedle-mediated transdermal delivery of biopharmaceuticals. Pharm. 2023;15:277–92. https://doi.org/10.3390/pharmaceutics15010277.
27. Donnelly RF, Prausnitz MR. The promise of microneedle technologies for drug delivery. Drug Deliv Transl Res. 2023;14:573–80. https://doi.org/10.1007/s13346-023-01430-8.
28. Dong S, Zhang Y, Zhang Y, Mei Y, Sina A, Zou R, Niu L. A novel multifunctional microneedle patch for synergistic photothermal- gas therapy against maxillofacial malignant melanoma and associated skin defects. J Nanobiotechnol. 2024;22:199–218. https://doi.org/10.1186/s12951-024-02409-4.
29. Wu T, Hou X, Li J, Ruan H, Pei L, Guo T, Wang Z, Ci T, Ruan S, He Y. Microneedle-mediated biomimetic cyclodextrin metal organic frameworks for active targeting and treatment of hypertrophic Scars. ACS Nano. 2021;15:20087–104. https://doi.org/10.1021/acsnano.1c07829.
30. Zhang Q, Shi L, He H, Liu X, Huang Y, Xu D, Yao M, Zhang N, Guo Y, Lu Y. Down-regulating scar formation by microneedles directly via a mechanical communication pathway. ACS Nano. 2022;16:10163–78. https://doi.org/10.1021/acsnano.1c11016.
31. Bi D, Qu F, Xiao W, Wu J, Liu P, Du H, Xie Y, Liu H, Zhang L, Tao J. Reactive oxygen species-responsive gel-based microneedle patches for prolonged and intelligent psoriasis management. ACS Nano. 2023;17:4346–57. https://doi.org/10.1021/acsnano.2c08979.
32. Zhang Y, Yin P, Huang J, Yang L, Liu Z, Fu D, Hu Z, Huang W, Miao Y. Scalable and high-throughput production of an injectable platelet-rich plasma (PRP)/cell-laden microcarrier/hydrogel composite system for hair follicle tissue engineering. J Nanobiotechnol. 2022;20:465–87. https://doi.org/10.1186/s12951-022-01671-8.
33. Wu X, Huang X, Zhu Q, Zhang J, Hu J, Song Y, You Y, Zhu L, Lu J, Xu X. Hybrid hair follicle stem cell extracellular vesicles co-delivering finasteride and gold nanoparticles for androgenetic alopecia treatment. J Control Releas. 2024. https://doi.org/10.1016/j.jconrel.2024.07.066.
34. Li Q, Wang Y, Guo Q, Cao J, Feng Y, Ke X. Nanostructured lipid carriers promote percutaneous absorption and hair follicle targeting of tofacitinib for treating alopecia areata. J Control Releas. 2024;372:778–94. https://doi.org/10.1016/j.jconrel.2024.06.060.
35. Yuan A, Gu Y, Bian Q, Wang R, Xu Y, Ma X, Zhou Y, Gao J. Conditioned media-integrated microneedles for hair regeneration through perifollicular angiogenesis. J Control Releas. 2022;350:204–14. https://doi.org/10.1016/j.jconrel.2022.08.007.
36. Zhou Y, Jia L, Zhou D, Chen G, Fu Q, Li N. Advances in microneedles research based on promoting hair regrowth. J Control Releas. 2023;353:965–74. https://doi.org/10.1016/j.jconrel.2022.12.040.
37. Cao S, Wang Y, Wang M, Yang X, Tang Y, Pang M, Wang W, Chen L, Wu C, Xu Y. Microneedles mediated bioinspired lipid nanocarriers for targeted treatment of alopecia. J Control Releas. 2021;329:1–15. https://doi.org/10.1016/j.jconrel.2020.11.038.

38. He Y, Andrade AF, Ménard-Moyon C, Bianco A. Biocompatible 2D materials via liquid phase exfoliation. Adv Mater. 2024;36: e2310999. https://doi.org/10.1002/adma.202310999.
39. Wei S, Xie J, Luo Y, Ma Y, Tang S, Yue P, Yang M. Hyaluronic acid based nanocrystals hydrogels for enhanced topical delivery of drug: a case study. Carbohydr Polym. 2018;202:64–71. https://doi.org/10.1016/j.carbpol.2018.08.112.
40. Xiao T, Li B, Lai R, Liu Z, Xiong S, Li X, Zeng Y, Jiao S, Tang Y, Lu Y, Xu Y. Active pharmaceutical ingredient-ionic liquids assisted follicular co-delivery of ferulic acid and finasteride for enhancing targeted anti-alopecia. Int J Pharm. 2023;648: 123624. https://doi.org/10.1016/j.ijpharm.2023.123624.
41. Yuan A, Xia F, Bian Q, Wu H, Gu Y, Wang T, Wang R, Huang L, Huang Q, Rao Y. Ceria nanozyme-integrated microneedles reshape the perifollicular microenvironment for androgenetic alopecia treatment. ACS Nano. 2021;15:13759–69. https://doi.org/10.1021/acsnano.1c05272.
42. Zhang X, Xi Z, Machuki JOa, Luo J, Yang D, Li J, Cai W, Yang Y, Zhang L, Tian J. Gold cube-in-cube based oxygen nanogenerator: a theranostic nanoplatform for modulating tumor microenvironment for precise chemo-phototherapy and multimodal imaging. ACS Nano. 2019;13:5306–25. https://doi.org/10.1021/acsnano.8b09786.
43. Sun B, Ye Z, Zhang M, Song Q, Chu X, Gao S, Zhang Q, Jiang C, Zhou N, Yao C, Shen J. Light-activated biodegradable covalent organic framework-integrated heterojunction for photodynamic, photothermal, and gaseous therapy of chronic wound infection. Acs Appl Mater Interfac. 2021;13:42396–410. https://doi.org/10.1021/acsami.1c10031.
44. Jung YH, Chae CW, Choi GE, Shin HC, Lim JR, Chang HS, Park J, Cho JH, Park MR, Lee HJ, Han HJ. Cyanidin 3-O-arabinoside suppresses DHT-induced dermal papilla cell senescence by modulating p38-dependent ER-mitochondria contacts. J Biomed Sci. 2022;29:17–33. https://doi.org/10.1186/s12929-022-00800-7.
45. Zhang Y, Huang J, Fu D, Liu Z, Wang H, Wang J, Qu Q, Li K, Fan Z, Hu Z, Miao Y. Transcriptome analysis reveals an inhibitory effect of dihydrotestosterone-Treated 2D- and 3D-cultured dermal papilla cells on hair follicle growth. Front Cell Dev Biol. 2021;9:724310–32. https://doi.org/10.3389/fcell.2021.724310.
46. Chaudary S, Karner L, Weidinger A, Meixner B, Rieger S, Metzger M, Zipperle J, Dungel P. In vitro effects of 635 nm photobiomodulation under hypoxia/reoxygenation culture conditions. J Photochem Photobiol B. 2020;209: 111935. https://doi.org/10.1016/j.jphotobiol.2020.111935.
47. Pan J, Ruan W, Qin M, Long Y, Wan T, Yu K, Zhai Y, Wu C, Xu Y. Intradermal delivery of STAT3 siRNA to treat melanoma via dissolving microneedles. Sci Rep. 2018;8:1117–27. https://doi.org/10.1038/s41598-018-19463-2.
48. Xiong M, Zhang Q, Hu W, Zhao C, Lv W, Yi Y, Wang Y, Tang H, Wu M, Wu Y. The novel mechanisms and applications of exosomes in dermatology and cutaneous medical aesthetics. Pharmacol Res. 2021;166: 105490. https://doi.org/10.1016/j.phrs.2021.105490.
49. Grams YY, Whitehead L, Cornwell P, Bouwstra JA. Time and depth resolved visualisation of the diffusion of a lipophilic dye into the hair follicle of fresh unfixed human scalp skin. J Control Releas. 2004;98:367–78. https://doi.org/10.1016/j.jconrel.2004.05.010.
50. Tolentino S, Pereira MN, Cunha-Filho M, Gratieri T, Gelfuso GM. Targeted clindamycin delivery to pilosebaceous units by chitosan or hyaluronic acid nanoparticles for improved topical treatment of acne vulgaris. Carbohydr Polym. 2021;253:117295–303. https://doi.org/10.1016/j.carbpol.2020.117295.
51. Guo Y, Zhang C, Xie B, Xu W, Rao Z, Zhou P, Ma X, Chen J, Cai R, Tao G, He Y. Multifunctional microneedle patch based on metal-phenolic network with photothermal antimicrobial, ROS scavenging, immunomodulatory, and angiogenesis for programmed treatment of diabetic wound healing. Acs Appl Mater Interfac. 2024;16:33205–22. https://doi.org/10.1021/acsami.4c07091.
52. Yi X, Duan QY, Wu FG. Low-temperature photothermal therapy: strategies and applications. Research. 2021;2021:1–38. https://doi.org/10.34133/2021/9816594.
53. Yin M, Zeng Y, Liu HQ, Zhang W, Wang C, Chen C, Li W. Dissolving microneedle patch integrated with microspheres for long-acting hair regrowth therapy. Acs Appl Mater Interfac. 2023;15:17532–42. https://doi.org/10.1021/acsami.2c22814.
54. Cuevas-Diaz Duran R, Martinez-Ledesma E, Garcia-Garcia M, Bajo Gauzin D, Sarro-Ramírez A, Gonzalez-Carrillo C, Rodríguez-Sardin D, Fuentes A, Cardenas-Lopez A. The biology and genomics of human hair follicles: a focus on androgenetic alopecia. Int J Mol Sci. 2024;25:2542–62. https://doi.org/10.3390/ijms25052542.
55. Shin DW. The molecular mechanism of natural products activating Wnt/beta-catenin signaling pathway for improving hair loss. Life Basel. 2022;12:1856–73. https://doi.org/10.3390/life12111856.
56. Zhu D, Wang S, Lawless J, He J, Zheng Z. Dose dependent dual effect of Baicalin and herb Huang Qin extract on angiogenesis. PLoS ONE. 2016;1:e0167125-0167142. https://doi.org/10.1371/journal.pone.0167125.
57. de Abreu Chaves ME, de Araujo AR, Cruz Piancastelli AC, Pinotti M. Effects of low-power light therapy on wound healing: LASER x LED. An Bras Dermatol. 2014;89:616–23. https://doi.org/10.1590/abd1806-4841.20142519.
58. Ceruti JM, Leirós GJ, Balañá ME. Androgens and androgen receptor action in skin and hair follicles. Mol Cell Endocrinol. 2017;465:122–33. https://doi.org/10.1016/j.mce.2017.09.009.
59. Khantham C, Yooin W, Sringarm K, Sommano SR, Jiranusornkul S, Carmona FD, Nimlamool W, Jantrawut P, Rachtanapun P, Ruksiriwanich W. Effects on steroid 5-alpha reductase gene expression of thai rice bran extracts and molecular dynamics study on SRD5A2. Biol Basel. 2021;10:319–41. https://doi.org/10.3390/biology10040319.
60. Jin SE, Kim J, Sung JH. Recent approaches of antibody therapeutics in androgenetic alopecia. Front Pharmacol. 2024;15:1434961. https://doi.org/10.3389/fphar.2024.1434961.
61. Choi BY. Targeting Wnt/beta-catenin pathway for developing therapies for hair loss. Int J Mol Sci. 2020;21:4915–30. https://doi.org/10.3390/ijms21144915.
62. Kwon YE, Choi SE, Park KH. Regulation of cytokines and dihydrotestosterone production in human hair follicle papilla cells by supercritical extraction-residues extract of Ulmus davidiana. Molecules. 2022;4:1420–3049. https://doi.org/10.3390/molecules27041419.

Publisher's Note